Chapter 5
Enabling Materials By Dimensionality: From 0D to 3D Carbon-Based Nanostructures

Simone Taioli

Abstract This chapter is aimed at analysing the influence that dimensional scaling exerts on the electronic, optical, transport and mechanical properties of materials using both experiments and computer simulations. In particular, to climb the "dimensional ladder" from 0D to 3D, we analyse a specific set of all-carbon allotropes, making the best use of the versatility of this element to combine in different bonding schemes, such as sp^2 and sp^3, resulting in architectures as diverse as fullerenes, nanotubes, graphene, and diamond. Owing to the central role of carbon in future emerging technologies, we will discuss a variety of physical observables to show how novel characteristics emerge by increasing or decreasing the dimensional space in which particles can move, ranging from the charge transport in semiconductor (diamond) and semimetallic (graphite) samples to the stress-strain characteristics of several 2D carbon-based materials, to the gas absorption and selectivity in pillared structures and to the thermal diffusion in foams. In this respect, our analysis uses ab initio, multiscale and Monte Carlo (MC) methods to deal with the complexity of physical phenomena at different scales. In particular, the response of the systems to external electromagnetic fields is described using the effective dielectric model of the plasma losses within a Monte Carlo framework, while pressure fields are dealt with the ab initio simulation of the stress-strain relationships. Moreover, in this chapter we present recent theoretical and experimental investigations aimed at producing graphene and other carbon-based materials using supersonic molecular beam epitaxy on inorganic surfaces, starting from fullerene precursors. We mostly focus on the computational techniques used to model various stages of the process on multiple length and time scales, from the breaking of the fullerene cage upon impact to the rearrangement of atoms on the metal surface used to catalyse graphene formation. The insights obtained by our computational modelling of the impact and of the following chemical-physical processes underlying the materials growth have been successfully used to set up an

S. Taioli (✉)
European Centre for Theoretical Studies in Nuclear Physics and Related Areas (ECT*), Trento, Italy
e-mail: taioli@ectstar.eu; http://www.ectstar.eu/people/profile/taioli

T. Onishi (ed.), *Theoretical Chemistry for Advanced Nanomaterials*,
https://doi.org/10.1007/978-981-15-0006-0_5

experimental procedure that ended up in the production of graphene flakes by C_{60} impact on copper surfaces.

Keywords Dimensionality · Carbon-based materials · Optical, electronic, andmechanicalproperties · Multiscalesimulations, synthesis, characterization

5.1 Introduction: The Course of Dimensionality

Dimensionality affects dramatically the physical properties of materials owing to the different way that Coulomb repulsion acts upon the electrons in three-dimensional (3D), two-dimensional (2D), one-dimensional (1D), and molecular (0D) structures. Indeed, the presence of constraints on the particle's motion in one or more degrees of freedom leads to remarkable consequences, such as quantum confinement, anisotropic characteristics and new phases. These effects can completely modify the properties that low-dimensional physical systems exhibit with respect to their bulk counterparts.

Additionally, quantum objects do interfere with one another, so that the quantum state of a many-body system is the result of the interaction between its constituent particles. This many-body potential depends on dimensionality and confinement and thus is much more than the simple sum of the interaction between its building blocks. This concept was masterly described by Philip W. Anderson in his article "More is different" [1], where he argues that "the behaviour of large and complex aggregations of elementary particles, it turns out, is not to be understood in terms of a simple extrapolation of the properties of a few particles. Instead at each level of complexity entirely new properties appear…". In this regard, for example, while at angstrom scale it is hard to differentiate between 0D point-like atomic species, such as tantalum or niobium, at 3D macroscale the former is a lustrous transition metal, and the latter undergoes a phase transition to a BCS-type II superconductor at 9.26 K. This means that at the time we reach the microscale, electrons of Nb pair up in Cooper pairs and condensate, transforming the material in a superconductor characterized by zero-resistance conductivity.

While intuitively one may think that increasing the number of degrees of freedom generally results in higher levels of complexity, at odds in physics and chemistry, the curse of dimensionality can act in one or another direction. In this book chapter, we will analyse quite a few examples of this "unconventional" scaling.

For instance, a relative simple approach to describe magnetic materials is provided by the Ising model [2]. This simplified mathematical model of solids represents real systems as made of atomic spins interacting with their neighbours on a lattice and can be used to identify phase transitions. According to the traditional solutions, there is no magnetization in the one-dimensional Ising model in the absence of external magnetic fields, while the two-dimensional square lattice is the simplest statistical problem to show a phase transition. In this respect, while the one-dimensional Ising lattice represents a relatively simple toy model in statistical

mechanics to be solved, the two-dimensional one is highly nontrivial. To date furthermore, the three- or higher-dimensional Ising problems remain unsolved although there exist different approaches related to quantum field theory to tackle this issue.

In more realistic systems, one needs to look no further than studies of the 2D electron gas in semiconductor heterostructures [3] or to the rich physics of graphene [4] and of layered hybrid materials [5] to find examples of remarkable as well often unexpected behaviour of low-dimensional systems. Indeed monolayers, which can be obtained by mechanical exfoliation of bulk crystals, have generally distinctive properties from their bulk counterpart. For example, while bulk MoS_2 in the 2H phase is an indirect band gap semiconductor, MoS_2 monolayer shows a direct band gap.

Moreover, the synthesis of stable cylindrical shapes in several material families, such as nanotubes and nanowires [6], has driven the discovery of completely novel extraordinary thermal, mechanical and electrical properties. Owing to their monodimensional shape, nanotubes and nanowires can be easily integrated in nanoscale devices and used efficiently in electron charge transport and optical excitations with potential applications in nanoelectronics, in composites and functional nanomaterials to enhance their mechanical properties, as well as drug delivers or in photodynamic therapy for cancer cure [7]. Carbon nanotubes in particular [8], owing to the material's exceptional strength and stiffness, have been synthesized with a length-to-diameter ratio of up to $132 \times 10^6 : 1$ [9]. Their electronic and optical properties are determined by the tube's chirality, which is a feature emerging from the 1D geometry inducing an exceptionally high excitonic binding energy [10–12].

By further miniaturizing a device, so to obtain quantum dots (0D) [13], one can observe several phenomena such as the Coulomb blockade due to the strong Coulomb repulsion in charge confinement and the electron tunneling which led to the concept of single-electron transistors [14]. Quantum dots have also been suggested as a possible mean of implementations of qubits for quantum information processing [15].

Another feature of low-dimensional systems is to show energetically discrete molecular-like bands due to confinement and, thus, a sharper density of states (DOS) with respect to higher-dimensional structures. In particular, they exhibit DOS singularities, thus having the potential for superior transport and optical properties with respect to their higher-dimensional counterparts [16]. For example, we sketch the typical DOS of 0D (dots), 1D (wires), 2D (wells) and 3D crystals in left panel of Fig. 5.1, where spikes emerge in the spectrum descending the dimensional ladder.

The fingerprint of dimensionality can be also found in the optical properties of solids. In particular, limiting the discussion to the interband transitions in a semiconductor at zero temperature, a radiation field impinging on a crystal can be absorbed at energies equal to the difference between valence and conduction bands, whereby an electron is excited to a higher energetic level with respect to its ground state. This information is encoded in the energy-dependent absorption coefficient, which in turn is proportional to the imaginary part of the energy-dependent dielectric function $\epsilon(\omega)$ [17]:

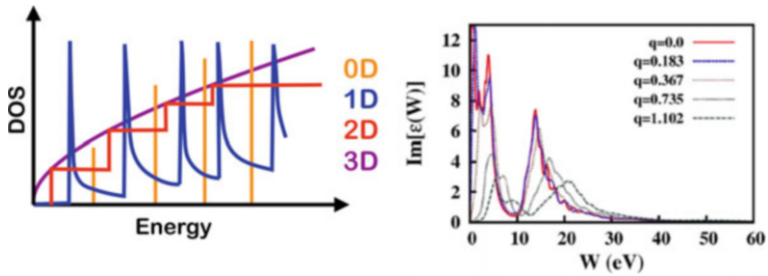

Fig. 5.1 Left panel: bulk 3D material (purple) shows typically continuous DOS, while 1D wires (blue) show van Hove singularities. Right panel: imaginary part of the graphite dielectric function vs. energy (eV) for different momentum transfer q (Å^{-1}) along the ΓL direction, obtained from ab initio simulations. (Reprinted from Ref. [18], Copyright 2017, with permission from Elsevier)

$$\alpha(\omega) = \frac{\omega}{nc}\Im(\epsilon) \tag{5.1}$$

where n is the ordinary refraction index and c is the speed of light in vacuum. The dielectric function is thus a fundamental quantity connecting microscopic observables, such as the band structure of the solid, with macroscopic features, such as the optical properties. The dielectric function is in particular related to the transition probability between a couple of valence and conduction bands, which is proportional to the joint density of states (JDOS) for slowly varying dipole matrix elements [17]. The JDOS provides a measure of the number of allowed optical transitions between the occupied valence and the unoccupied conduction bands separated by photon energy $\hbar\omega$. This is why the JDOS is usually related to the energy-dependent absorption coefficient of Eq. 5.1. Thus, while the DOS counts the number of electronic states at a given energy, the JDOS encloses information on the optical properties, and it is defined as the convolution of the valence and conduction band DOS which are linked by optical transitions. In 3D crystals the JDOS shows four different critical points (maximum, minimum and two saddle points), which tend to have square root singularities. The JDOS in 1D is not a continuous function of energy but presents sharp discontinuous spikes in contrast to three-dimensional materials, showing singularities near the critical points with a behaviour equal to the square root inverse of the energy. At odds, in the two-dimensional case, one identifies three critical points of the JDOS (maximum, minimum and one saddle point), and at the saddle point, the latter is logarithmically divergent, so more easily detectable in experiments where of course these divergences are smoothed out by the electron-electron interactions. In the right panel of Fig. 5.1, we report the optical excitation spectrum for different transferred momenta (proportional to $\Im(\epsilon)$ as by Eq. 5.1) of graphite, which is a quasi-2D materials, where the van Hove singularities are clearly visible.

Dimensionality leaves its signature also in several other observables, such as in plasmon excitations and in the quantum Hall effect in low-dimensional systems.

The former represents a tool for coupling and transferring energy. This mechanism depends on the dimensional scale. Indeed, contrary to ordinary surface plasmons of bulk materials, in low-dimensional structures, plasmon dispersion goes to zero in the long wavelength limit, covering an energy range from terahertz to near infrared. Moreover, in layered materials their in-plane dispersion, such as in the case of transition metal dichalcogenides, can show a negative in-plane plasmon dispersion [19]. Quantum Hall effect in low-dimensional materials, e.g. in graphene, is different from the spin Hall effect found in 3D systems, as it leads to a phase which is topologically distinct from a band insulator [20].

So far, according to the abovementioned Anderson's conjecture, we have shown examples in which the dependence on dimensionality of the particle-particle correlation plays a crucial role. Nevertheless, in some occasions a dimensional change can be enough to modify dramatically the behaviour of physical systems, despite correlation among constituents is switched off.

For example, let us analyse the effect that a dimensional change has on the electronic properties of a system of free (noninteracting) electrons. This model, which is called *Fermi gas*, is appropriate to study the conduction in simple systems, such as alkali and noble metals, even though rigorously the electron motion is also influenced by the periodic potential created by the ions in the lattice. By solving the Schrödinger equation for one electron in a box of edge L where periodic boundary conditions are introduced, a set of discrete energy levels $E_n = \frac{\hbar^2}{2m}(\frac{2\pi n_{x,y,z}}{L})^2 = \frac{\hbar^2}{2m}(k_{x,y,z})^2$ emerge, where $n_{x,y,z}$ is an integer number, m is the electron mass, $\hbar$ is the reduced Plank constant, and $k_{x,y,z}$ is the corresponding wavevector along the three Cartesian directions x, y, z. By neglecting the electron-electron interactions, we can build up the N-electron ground state of the system by accommodating the charges into the allowed one-electron levels starting from the bottom, provided that the same state cannot be occupied by more than two electrons, one with spin up and one with spin down orientation. Indeed, electrons are fermions, following the Fermi-Dirac statistics, and obey the Pauli's exclusion principle. The occupied orbitals are represented by a point in the k-space inside a sphere of radius $k_F = \sqrt{2m\epsilon_F/\hbar^2}$, which is the highest momentum an electron can have within the box. ϵ_F is the Fermi energy, which defines the so-called Fermi sphere, within which all occupied one-electron levels lay. The number of electronic states per unit energy range (DOS, $D(\epsilon)$) in the solid is a quantum observable: for Al, for example, one has $\epsilon_F = 11.6\,\text{eV}$ and $D(\epsilon_F) = 0.39\,(\text{eV atom})^{-1}$.

Furthermore, the kinetic energy of the electron gas increases with temperature, and some energy levels, which were vacant at 0 K, start to be populated. The distribution of electrons among the levels is described by the Fermi distribution function, $f(E) = 1/(\exp^{(\epsilon-\mu)/k_B T} + 1)$, which gives the probability that the energy level E is occupied by fermions. Multiplying the DOS by the latter function, one can obtain the DOS analytic expressions for electrons at temperature T confined in their motion by infinite barriers into (i) a cube box of side L (3D), (ii) a square surface of side L (2D) and (iii) a wire of length L (1D), as follows:

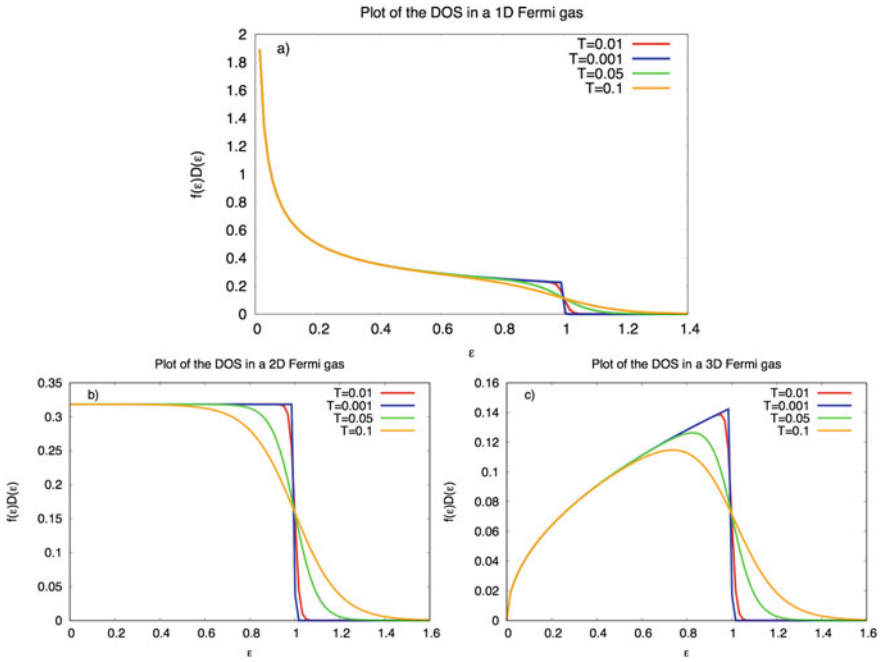

Fig. 5.2 DOS (y-axis) of a free Fermi gas at different temperatures T confined into (**a**) 1D, (**b**) 2D, and (**c**) 3D dimensions vs. energy (x-axis). The electronic levels are populated according to the Fermi distribution function $f(\epsilon) = 1/(\exp^{(\epsilon-1)/T} + 1)$, where the chemical potential $\mu = 1$ is assumed independent of temperature T, and $k_B = 1$. The constant in front of the analytical expression of $D(\epsilon)$ (Eq. 5.2) is assumed equal to 1

$$f(\epsilon)D(\epsilon) = f(\epsilon) \begin{cases} \frac{L^3}{2\pi^2}\left(\frac{2m}{\hbar^2}\right)^{3/2}\epsilon^{1/2}, \ in\ 3D \\ \frac{mL^2}{\pi\hbar^2}, \ in\ 2D \\ \frac{L}{\pi}\left(\frac{2m}{\hbar^2}\right)^{1/2}\epsilon^{-1/2}, \ in\ 1D \end{cases} \tag{5.2}$$

In Fig. 5.2a–c, we report the plots of the DOS for 1D-, 2D- and 3D-confined free Fermi gas at several finite temperatures. Of course, also other quantities derived from the DOS, such as the chemical potential μ, are affected by dimensionality.

While the potential for quantum matter to develop emergent properties is far more striking, nevertheless also classical objects, such as the natural systems, can feel the course of dimensionality and exhibit new classes of behaviour upon dimensional scaling. In particular, the principle that drives the action of systems in nature is the same of quantum objects: behaviour cannot be rationalized as the simple sum of their building block's activity. Nature's great lesson in this regard is that structural solutions of biomaterials at different length scales and dimensions, from nano- to micro- and macro-architectures, are optimized according to hierarchies, in which the building blocks are organized so to "do more with less".

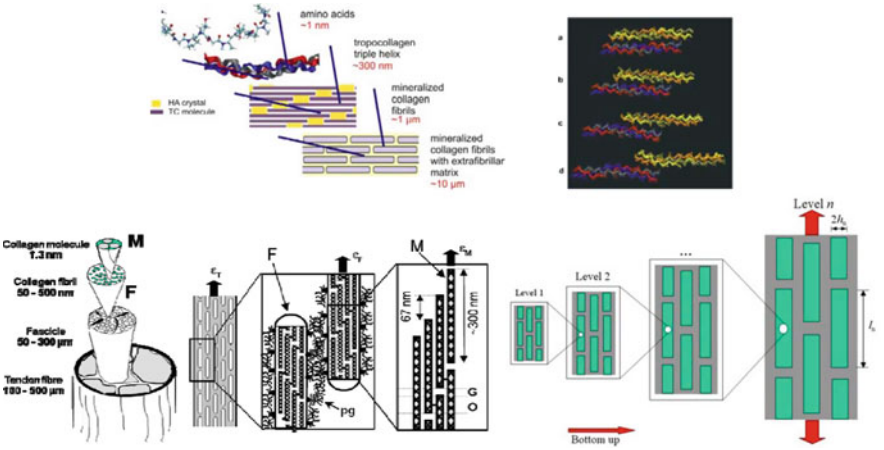

Fig. 5.3 Hierarchical structures of bones and tendons. (Adapted from Refs. [21–24] with permission)

Complex behaviour and functionalities can emerge from the way constituents are assembled or interact with one another, in such a way that the optical or mechanical response of biomaterials to external electromagnetic or force fields is dramatically influenced, or even completely modified, by the presence of these hierarchical levels (see Fig. 5.3 reporting the hierarchical levels present in human tendons). This is of course the result of the basic mechanisms of evolution that nature developed over the years in order to have robust and flaw-tolerant structures for survival. This hierarchical (or dimensional) effect can be seen in many natural systems, e.g. spider silk, gecko feet, lotus flower, bones, tendons (see Fig. 5.3 [21–24]) or butterfly wings to cite a few.

On the other side, even in the realm of real-world technological materials, the electronic, optical and mechanical properties are also affected by dimensionality. One of the most striking examples in this regard is provided by the large family of carbon-based materials. Indeed, carbon is one of the most versatile chemical elements: its relatively small atomic radius and the tetravalent character mean that carbon can easily form covalent bonds with several chemical elements, including itself, also at room conditions. This is the very reason why the number of known chemical compounds constituted of carbon – which is only the 4th most abundant element in the universe by mass after hydrogen, helium and oxygen and only the 15th most abundant in the Earth's crust – is by far higher than the sum of all the others (in excess of 10 million). For example, at odds, silicon is another element in group 14 of the periodic table having also four valence electrons which can bind into both molecular and crystalline compounds. However, due to its atomic radius, 1.5 times larger than that of carbon is too big to fit together into as great a variety of molecules as carbon atoms can.

This remarkable ability of carbon to bind in different ways by sharing from one single to four electrons may lead to the formation of single to triple bonds. This makes for an enormous number of possible bond combinations forming straight chains, such as polymers; rings, such as aromatic hydrocarbons; crystals, such as silicon carbide; and also amorphous phases. The all-carbon materials that carbon can form by binding in different ways are called allotropes of carbon, be those naturally available or man-made. The most common are graphite, diamond, fullerene and amorphous carbon. In this chapter, we will focus on the description of the physical properties of carbon allotropes with the aim to show how the dimensionality leaves its signature on the electronic, optical and mechanical properties of these carbon-based materials. For example, on the one side, graphite is a quasi-two-dimensional material whose distinctive treats are to be opaque, black and sufficiently soft to be used in pencils. Furthermore, graphite is a good electrical conductor. On the other side, diamond is a 3D transparent, hard solid showing low electrical conductivity. Nevertheless, at room conditions, 3D diamond, 1D carbon nanotubes, and 2D graphene have all large thermal conductivities.

In the discussion of these topics, we have made the disputable choice of focussing on the description of structures which grown out of our research activity over the last decade. This includes the fullerenes' family (0D), carbon nanotubes (1D), graphene sheets (2D) and other two-dimensional allotropes, graphite (quasi-2D) as well as diamond and foams (3D) (see Fig. 5.4). This thorough analysis will also show how the investigation of these structures stimulated the development of new computational tools with the ambition to connect first-principles, atomistic,

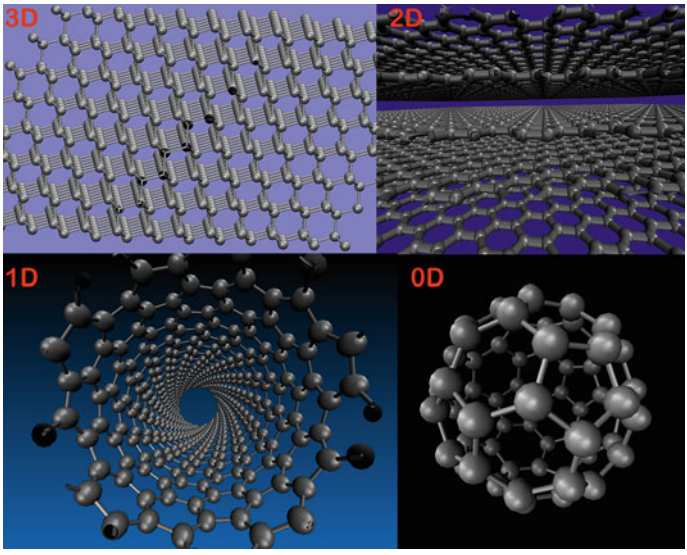

Fig. 5.4 Allotropes of carbon. From left to right: diamond (3D); graphene (2D); nanotubes (1D); and buckyballs (0D)

mesoscopic and continuum models to integrate different levels of simulation for climbing the "dimensional ladder". This approach is not surprisingly called multiscale analysis.

5.2 0D Carbon Materials: The Fullerenes

Pristine C_{60} or buckminsterfullerene is a 0D all-carbon structure (molecule) made of 20 hexagonal and 12 pentagonal faces, with a carbon atom at the vertices of each polygon interconnected by bonds along each edge [25]. This amounts to 60 carbon atom vertices, connected via 90 covalent bonds among single (60) and double (30) bonds. C_{60} resembles a soccer ball (see bottom right panel of Fig. 5.4) and is shaped as a truncated icosahedron. Carbon atoms in C_{60} fullerene are equivalent, and their s and p outer shells are sp^2 hybridized (or almost like that if one refers this hybridization to planar-only geometries). The p orbitals, which are orthogonal to the hypothetical sphere inscribed in the fullerene, form π-type bonds.

While theoretical predictions [26] of the existence and stability of buckminsterfullerene were already put forward, the first isolated and characterized structure belonging to the fullerines' family was synthesized in 1985 by R.F. Curl, H.W. Kroto and R.E. Smalley [27]. Fullerene is the by-product of two synthesis methods, that is, the arc and the combustion methods, and sublimates below 800 °C. They own their name to Buckminster Fuller, an American architect universally known for his innovative design of the geodesic domes shaped as buckyballs.

Nevertheless, some evidence can be found that its geometrical shape was already postulated by Archimedes among his thirteen solids. To the best of author's knowledge, the oldest picture of the fullerene's structure dates back to the Italian renaissance painter and mathematician Piero della Francesca, who drew the shape of C_{60} in his book *Libellus de quinque corporibus regularibus* (see Fig. 5.5a). A further rendition of the truncated icosahedron, ascribed to Leonardo da Vinci, can be found in the book *De Divina Proportione*, written by Luca Pacioli around the end of the fifteenth century (see Fig. 5.5b).

The existence and stability of C_{60} are confirmed by mass spectrometry experiments, which show discrete peaks corresponding to molecules with the exact mass of 30 to 90 carbon atoms (see Fig. 5.6a [28]), making buckminsterfullerene one the most abundant molecules among the fullerenes' family. Furthermore, we report in Fig. 5.6c the relative cohesive energies of carbon architectures at different dimensionality, including linear chains, rings, 2D flakes and fullerenes, which are sketched in Fig. 5.6b. We notice that fullerenes are more stable than rings and planar flakes for $n > 20$, due to the absence of edges with respect to other 2D and 1D structures. Nevertheless, due to the constant positive curvature, which induces stress into the structure, fullerenes are not totally unreactive at odds with the planar sp^2 carbon net of graphene. They have been actually functionalized by several chemical elements, such as hydrogen [31], fluorine, bromine and chlorine [32], both in the

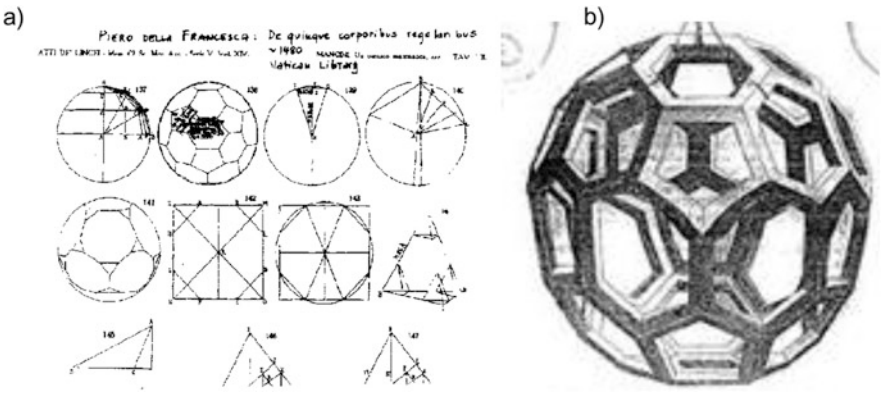

Fig. 5.5 (**a**) Rendition of a truncated icosahedron from the book *Libellus de quinque corporibus regularibus* by Piero della Francesca. (**b**) Fullerene geometry drawn by Leonardo da Vinci found in the *De Divina Proportione* by Luca Pacioli

outer and inner cage; $C_{61}Ph_2$ derivatives were prepared through cyclopropanation for use in organic solar cells [33].

Due to their symmetry, not belonging to the group of the perfect sphere, fullerenes are diamagnetic and display rather high electron affinity, and they do not conduce. At room conditions C_{60} is a semiconductor, with a band gap of about 2.3 eV [34], well reproduced by GW simulations reporting a band gap equal to 2.15 eV [35, 36], showing aromaticity but not "super-aromaticity" (see Fig. 5.7 for band structure and electron spectroscopy characterization). This means that for symmetry reasons, the electrons are not delocalized overall in the molecule whereas localized on the pentagons and the hexagons.

C_{60} usually is found in solid form, with buckyballs arranged in face-centred cubic configurations ($Fm3m$ symmetry group [37]) with lattice constant equal to 1.411 nm, kept together via van der Waals intermolecular forces (see Fig. 5.8). Fullerenes are thus weakly interacting, and the valence bands are only slightly deviated from those of the isolated icosahedral. In Fig. 5.7, we report the electronic structure of the C_{60} cluster (top left panel) and of the fcc solid fullerite (top right panel) [38], along with the photoelectron spectroscopy (PES) and the electron energy-loss spectroscopy (EELS) experimental measurements of thin films of solid C_{60} [39]. We notice that the unique electronic properties of fullerenes have been used to produce molecular rectifiers and transistors that can operate with more than two logical states [40]. Doping with alkali metals leads to compositions such as M_3C_{60} (M can be K, Rb or Cs), called fullerides, which display also superconductive behaviour at low temperature [41].

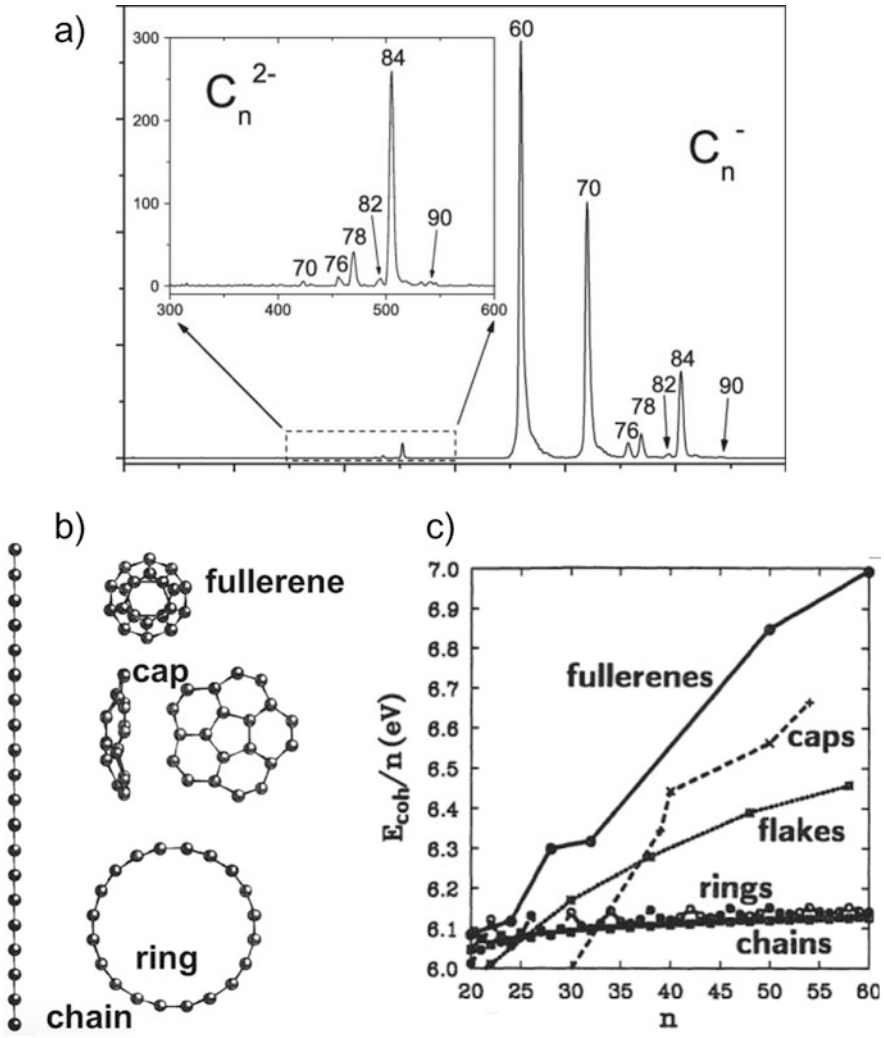

Fig. 5.6 (**a**) Time-of-flight mass spectrum of fullerenes. The mass of C_{60} is 720 amu; (**b**) linear chains, rings, caps and fullerenes structural arrangements; (**c**) binding energy per atom E_{coh}/n in different structural arrangements of C_n. (Panel (**a**) is reproduced from Ref. [28] with the permission of the European Physical Society, while panels (**b**)–(**c**) are reprinted with permission from Refs. [29, 30] Copyright 1991, 1992 by the American Physical Society)

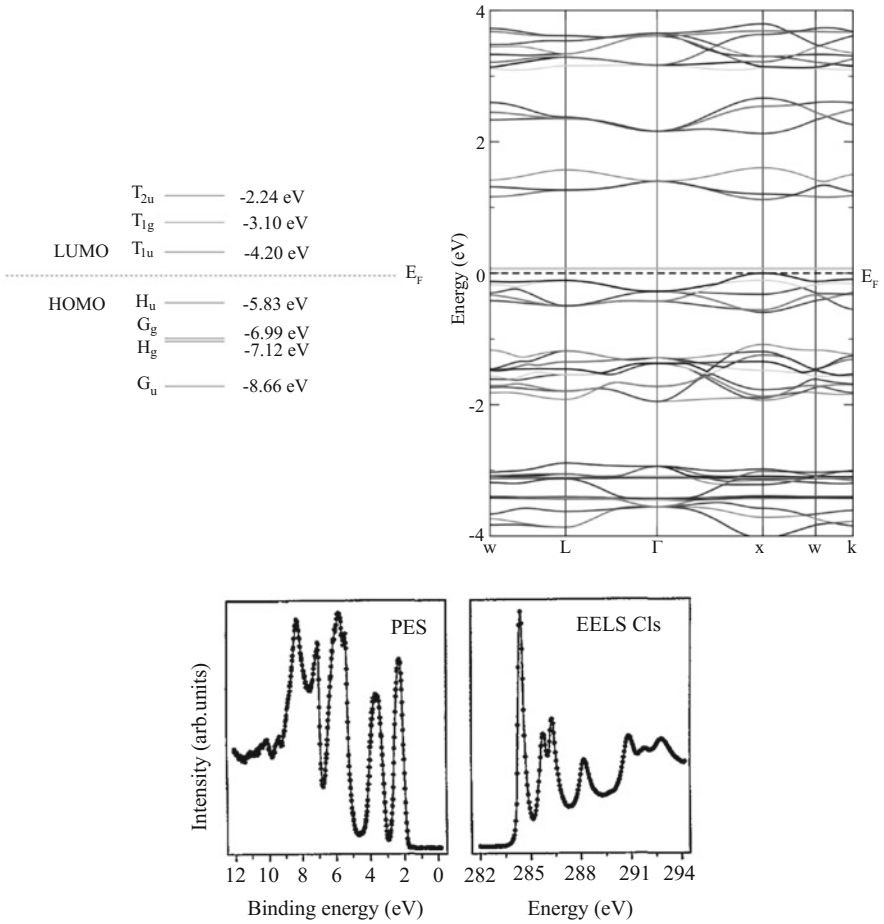

Fig. 5.7 Top panels: electronic structure of the C_{60} molecule (left) and of the pristine fullerite (solid fcc) within PBE-GGA+DFT-D3(vdW). Fermi levels of the two systems are aligned. (Adapted by permission from Springer Nature: [35], COPYRIGHT (2016)). Bottom: photoemission spectrum (left-hand panel, $h\nu = 21.22$ eV) and C 1 s excitation spectrum (right-hand panel) of a thin film of fullerenes. (Adapted from Ref. [39] with permission of UvA-DARE)

5.2.1 Using 0D Carbon Systems to Synthesize 2D Monolayers

The mechanical stability of fullerenes along with their massiveness, compactness and fair reactivity can suggest their use as precursors to initiate the growth of carbon-based materials. In this section we describe a novel experimental method able to grow materials using a kinetically driven approach at temperatures lower than those achieved so far by commonly adopted synthesis techniques.

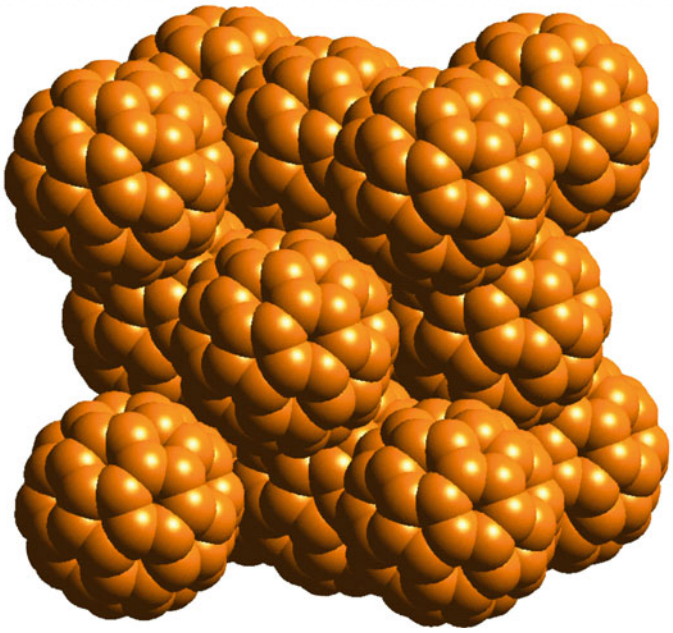

Fig. 5.8 FCC structure of solid C_{60}

In particular, we present recent theoretical and experimental advances on the epitaxy of graphene, when the appropriate molecular bonds are severed by impacting supersonic molecular beam of fullerenes on inorganic surfaces (SuMBE) [42–45]. Furthermore, we show how computational modelling can help our understanding of the various stages of the process on multiple length and time scales, from the breaking of the fullerene cage upon impact to the rearrangement of atoms on the metal surface used to catalyse graphene formation. We notice that the insights obtained by our simulations of the impact and following chemical-physical processes have been successfully used to set up an experimental procedure that ended up in the production of graphene flakes by C_{60} impact on copper surfaces [46].

Graphene is typically synthesized by chemical vapour deposition (CVD) of carbon-rich molecules (usually alkanes, such as propane) on metals [47, 48], such as nickel or copper. On the latter the growth of graphene is known to proceed by surface adsorption as carbon shows low solubility at high temperature [49]. Chemical reactions occurring on the surface are catalysed by the substrate, at temperatures higher than $\simeq$700 °C, and result in bond breaking and rearrangement into a two-dimensional extended structure [49, 50]. Given the presence of hydrogen atoms in the precursors and the relatively high working temperature, this process generally leads to defected hydrogenated graphene. A subsequent thermal treatment at about 1000 °C is finally used to desorb hydrogen, leaving graphene in a highly polycrystalline form.

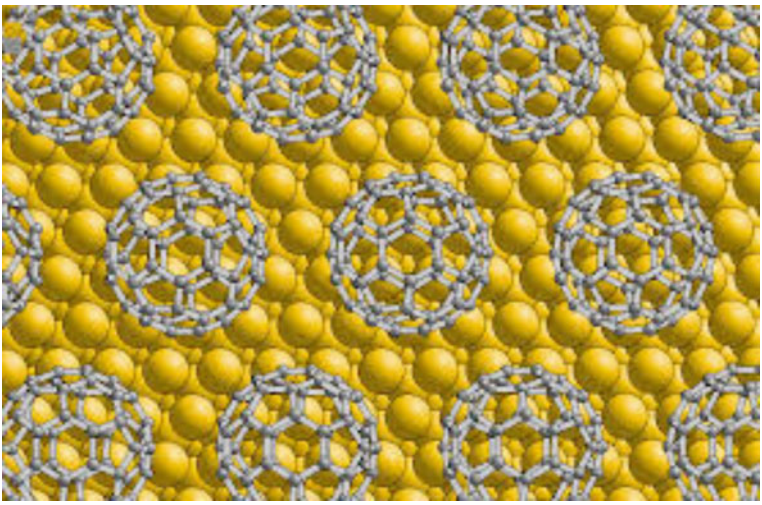

Fig. 5.9 Fullerenes on the top of metallic substrate

At variance, our procedure uses supersonic beams of C_{60} to induce the catalysis. Of course there is no way that by placing fullerenes on the top of a metallic substrate graphene can be formed (see Fig. 5.9). Instead, C_{60} cage must be somehow broken to trigger graphene growth. We remind that fullerenes have the shape of soccer balls, so they can be easily accelerated at intermediate to high kinetic energies (from a few to tens of eV) towards the substrate. On the one side, the high kinetic energy impacts provide the activation energy necessary to initiate graphene sheet formation, so one can avoid the typical shortcomings of CVD, such as the high-temperature dehydrogenation process. On the other side, this kinetic energy regime allows one to avoid crater formation, surface spreading and sputtering upon collision events.

Following this remarkably simple idea of bombarding a silicon substrate with buckyballs travelling at supersonic speeds (C_{60} kinetic energy = 35 eV), we were able to grow silicon carbide (3C-SiC) nanocrystalline islands (about 10 nm wide) with a completely relaxed lattice at room temperature (RT) using H_2 as carrier gas [42–45]. SiC island formation was also obtained at 800 K for a C_{60} kinetic energy (KE) of 20 eV using He as carrier gas. These experimental evidences show that (i) the chemical-physical mechanisms underlying SiC synthesis are kinetically driven and triggered by C_{60} cage disruption occurring above a KE threshold; (ii) SuMBE is a promising technique able to reduce drastically the growth temperature and increase the structural order.

5.2.1.1 Experimental Results

The experimental activity was focussed on synthesizing nanostructured carbon-based materials, such as silicon carbide (3C-SiC) [42–44] and graphene [46, 49, 50], using C_{60} fullerene supersonic beams impinging on metallic or semiconductor substrates aiming at room temperature (RT) growth conditions (see Fig. 5.10a). SuMBE makes use of two types of devices: one for producing a highly energetic beam of C_{60} molecules and the other for characterizing the growing film by in situ electron spectroscopy techniques. The apparatus is self-contained within a UHV chamber (base pressure = 7.0×10^{-11} mbar) and consists of a quartz tube in which an inert carrier gas, usually He or H_2, is seeded with highly diluted (below 0.1% in number of the mixture) organic molecules sublimated by Joule heating. Figure 5.11a shows a layout of the instrumentation under consideration.

In the case of graphene growth by SuMBE, the two major issues to take into account are the substrate type and the fullerene KE able to trigger the cage

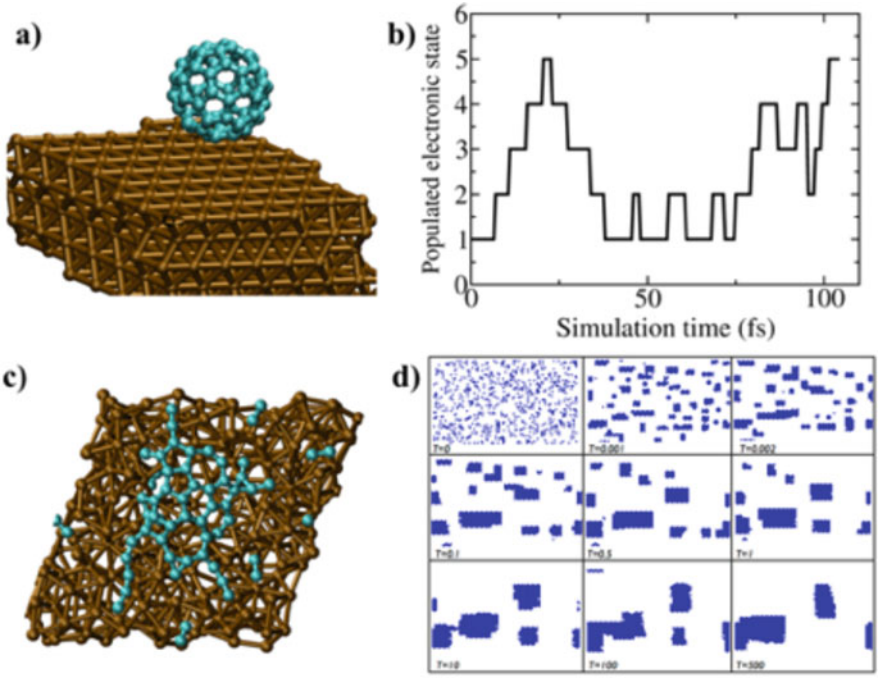

Fig. 5.10 (**a**) Representation of the system studied. A C_{60} molecule (cyan) and the Cu(111) surface (brown). (**b**) Time-dependent populated electronic state vs. simulation time. In particular, we report the first six electronic excited states (labelled from 1 to 6) above the ground state (labelled by 0) visited during a simulation of fullerene impact onto the Cu(111) surface. (**c**) Early stage investigations of graphene formation by metadynamics. (**d**) Kinetic Monte Carlo simulations of graphene flakes formation and merging by carbon diffusion on the Cu(111) surface. (Adapted from Refs. [46, 50])

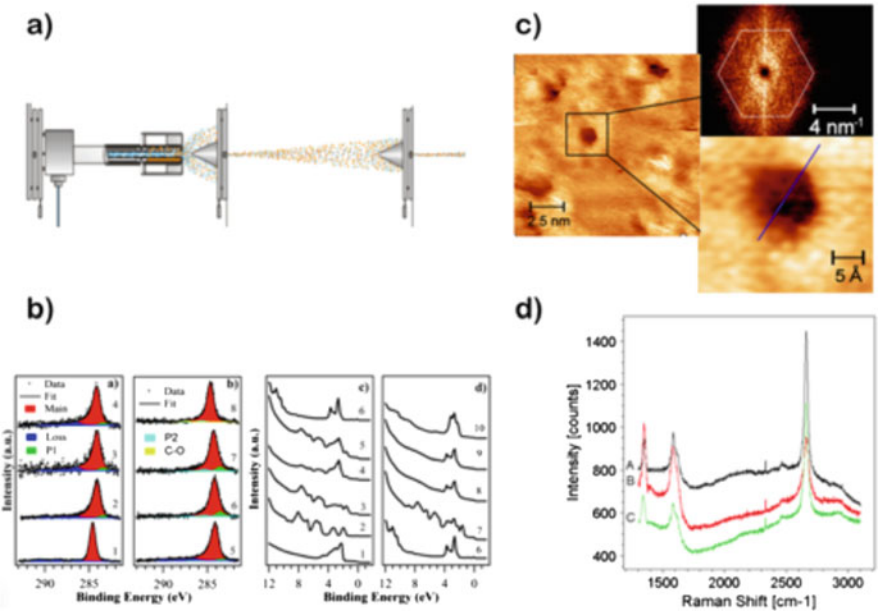

Fig. 5.11 (**a**) Schematic drawing of an apparatus for SuMBE deposition; (**b**) XPS and UPS measured spectra. Left panel: C1s CL from C_{60} film deposited at RT by SuMBE on Cu poly at KE = 15 eV (panels 1 and 2) and Cu(111) at KE = 35 eV (3, 4) with thickness: (1) 20 nm; (2) 1 ML; (3) 0.3 ML; (4) 0.6 ML.; C1s CL from C_{60} 1 ML films deposited at RT for KE = 35 eV, after thermal annealing at 425 °C (5), 645 °C (6), 795 °C (7). C1s emission from commercial single-layer graphene on Cu foil is shown for comparison (8). Right panel: VB on Cu poly (1); VB analysis of C_{60} films deposited by SuMBE on Cu poly at RT for KE=15 eV (2–3) and Cu(111) at KE = 35 eV (4, 5) with thickness: (2) 20 nm; (3) 1 ML, after annealing a 20 nm film at 400 °C; (4) 0.3 ML; (5) 0.6 ML. VB on Cu(111) (6); VB from C_{60} 1 ML film deposited at RT with KE = 35 eV, after thermal annealing at 425 °C (7), 645 °C (8), 795 °C (9). VB from a commercial graphene single layer on Cu foil (10) is shown for comparison. (**c**) STM analysis, showing few nm extended graphene-like domains after annealing at 645 °C a C_{60} 1 ML on Cu(111). (**d**) Raman analysis of C_{60} 1 ML on Cu(111) after annealing at 645 °C. A, B, C represent Raman spectra acquired in different regions of the sample. (Adapted from Ref. [46])

disruption. The main steps generally undertaken for synthesizing graphene via SuMBE (or also SiC thin films for which this technique was initially successfully used) are the following:

- **Surface preparation.** Several (up to 40) argon ion sputtering (0.5 keV) cycles and annealing of the copper substrate (T > 700 °C for obtaining optimal LEED diffraction pattern) to expunge contaminants, such as oxygen, sulphur or adventitious carbons.
- **Carrier gas choice.** C_{60} KE can be tuned by changing the carrier gas from He (lower KE) to H_2 (higher KE), being the KE inverse proportional to the carrier gas mass; furthermore, using noble gases a strong interaction with the substrate

leading to adsorption of the carrier gas is avoided. C_{60} internal dynamics is frozen unlike ordinary heating that dramatically increases the molecular vibrations.
- **Aerodynamical acceleration.** The highly diluted C_{60} plus carrier gas mixture fluxes via isentropic expansion out of the injection cell into vacuum through a nozzle (see Fig. 5.11a). Fullerene KE can be tuned not only by changing the carrier gas but also modifying the seeding parameters, such as the source temperature and the gas inlet pressure. In this way C_{60} KEs of 10–15 eV using He carrier gas can be achieved, while up to 30–40 eV using H_2.
- **Collimation** of the diluted mixture towards the copper reconstructed surface. The substrate temperature can be increased as well from RT conditions.
- **Thermal activated growth** of graphene islands by increasing the substrate temperature to 645 °C.

To our surprise, we found out that the substrate temperature must be raised to synthesize graphene islands as C_{60} high-energy deposition on Cu, even at the highest KE reachable by SuMBE, does not lead to immediate C_{60} cage rupture at variance with SiC growth on silicon (as confirmed by our nonadiabatic molecular dynamics simulations that find a KE cage breaking on copper higher than 40 eV). It seems that the excess of energy made available by C_{60} supersonic impacts is spent for rearranging fullerene positions in a very stable 4×4 pattern on the copper surface, which eventually induces a tighter interaction characterized by charge transfer between a number of carbon atoms of the organic molecule with the directly facing copper adatoms [51]. This covalent interaction at the C_{60}-Cu interface, following the 4×4 reconstruction, leaves its signature in our in situ core-level analysis, resulting in a spectral shift of about -0.5 eV and in the emergence of a new feature with respect to films deposited by standard MBE technique, at variance characterized by C_{60} clustering. These spectral characteristics, present at all beam KEs, at any surface coverage from 0.3 to 1 equivalent monolayers (ML), without remarkable differences for temperatures up to 445 °C, have been interpreted as the proof of a significant deformation, operated by the impinging C_{60} molecules, of the copper superficial layers into a cup shape with removal of a number of copper adatoms and formation of stable bonds with those surrounding the deformed or partially broken cage.

Moreover, we did not find evidence of C_{60} cage rupture by SuMBE deposition on single- or polycrystal copper in all range 10 to 40 eV, changing the carrier gas, even increasing the substrate temperature during the C_{60}-Cu collision up to 565 °C. Nevertheless, the 4×4 rearrangement of fullerenes on the copper surface induced by the collision creates favourable conditions for cage unzipping via thermally activated processes.

In fact, high-energy 4×4 deposition on single- or polycrystal substrates kept at RT, followed by a temperature increase to 550 °C (645 °C) when using He (H_2) as carrier gas, resulted in a dramatic change of the C_{60} typical spectral patterns (as seen in Fig. 5.11b). In particular, the main peak in the C1s core-level spectrum, not compatible with the presence of unbroken C_{60}, shows the typical asymmetry of defected graphene nano-islands, while the valence spectrum loses all the features

reported for the MBE deposited C_{60} film. Finally, the KVV Auger signal intensity from carbon is not depleted with respect to the copper one by increasing the temperature up to 800 °C, meaning that the grown species is stable and not volatile. Most importantly, evidence of fullerene cage disruption under these conditions has been found independently of the carrier gas used and of copper surface coverage from 0.3 to 1 ML.

The ultimate evidence of the presence of defected nanometric graphene islands on the copper substrate is confirmed by both STM measurements and Raman spectroscopy, reported in Fig. 5.11c, d, respectively.

These findings point towards a graphene growth model, in which the excess of energy provided by the C_{60} translational KEs does not lead immediately to C_{60} cage break and to the activation of kinetically driven chemical-physical mechanisms; rather, at odds with the case of SiC synthesis, this energy is used to enhance surface mobility and C_{60} diffusion, regardless of the carrier gas used for the expansion. Moreover, after fullerenes find their optimal hosting sites by lattice distortion of the copper surface owing to this increased mobility and tighten their interaction by forming covalent bonds with the inorganic substrate, chemical-physical processes that change the material topological and electronic properties can be thermally activated by raising the substrate temperature, eventually leading to the C_{60} cage break. The increase of temperature can of course enhance the catalytic action of copper as well as contribute to activate nonlinear excitations of vibrational motion and to desorb physisorbed species above the first C_{60} ML.

5.2.1.2 Computational Modelling: Breaking the Fullerene Cage

In this section, we report the principal computational results and modelling tools that have been used to model the physical-chemical processes leading from C_{60} impacts onto metallic surfaces to the early stages of graphene formation. A very similar theoretical and computational framework could be used to model the interaction with other surfaces commonly used in graphene synthesis, such as nickel, or to understand, and thus control, the growth of other carbon-based nanoclusters. However, due to the possible formation of nickel carbide species, we opted for single- or polycrystal copper substrates for which the chemical-physical mechanisms underlying graphene growth turned out to be very similar.

Previous calculations based on empirical or semiempirical interaction potentials [52, 53], aimed at investigating the stability of C_{60} molecules upon impact on silicon surfaces, indicate that KEs of several hundred of eV are required to observe cage rupture. However, this result was in sheer contrast with our experiments [42, 43], showing SiC formation on the surface of silicon for impinging KEs of $\simeq$ 35 eV at RT conditions. A detailed analysis of fullerene cage breaking conditions upon impact on the silicon substrate at different levels of accuracy (and corresponding different computational costs), using both classical and Born-Oppenheimer (BO) ab initio molecular dynamics (AIMD), confirmed these previous findings. Indeed, no cage breaking was observed for fullerene initial KEs lower than 300 eV, even

using first-principles molecular dynamics based on density functional treatment of the electronic motion [43].

While this conclusion is expected when using classical molecular dynamics, whereby atoms are treated as hard spheres interacting through a pair-wise potential, making this model not capable of treating out-of-equilibrium conditions where bonds are breaking and forming, it is surprising when electronic motion is explicitly treated from first-principles. However, a critical reassessment of the validity of the BO approximation – that is the assumption that the electrons at every instant collapse into their ground state configuration – suggests that the electronic and nuclear motion are intimately intertwined, due to the short time scales involved in the molecule-surface collision.

Indeed, computer simulations allowing electron hopping between several excited states, calculated by time-dependent density functional theory (TDDFT), indicate that C_{60} cage breaking can indeed occur for impact KEs of the order of 35 eV. Figure 5.10b shows the progressively higher-energy surfaces visited by the electrons during the simulation of a fullerene molecule approaching the silicon surface. Due to the high-energy impact occurring in the timespan of a few femtoseconds, electrons cannot relax fast enough to the ground state relative to the instantaneous configuration of the nuclei. Thus, the forces acting on the nuclei during molecular dynamics simulation must be calculated on the pure adiabatic surfaces populated at the present time step. These gradients can be very different from the BO ground state ones, leading to a highly dissociative path. Therefore, the cage disruption cannot be accurately modelled at the measured KE if not by adopting a nonadiabatic description of the impact. A similar behaviour was observed in the case of fullerene molecules breaking upon impact on copper surfaces: we found out that one needs to include excited-state dynamics in the description of the system in order to accurately describe the processes involved in the collision and correctly estimate the cage rupture energy threshold [46].

Similarly to what occurs with semiconducting silicon surfaces, even in the case of collision with copper surface, C_{60} cage breaking is observed for KEs slightly higher than 40 eV. Unfortunately, this KE is marginally too high for SuMBE. In the experimental section, we have seen indeed that in order to synthesize graphene islands, we need to raise the substrate temperature up to 645 °C after the impact.

It is worth noticing that the significant computational requirements of excited-state simulations prevent following the system's dynamics on time scales much larger than several hundred femtoseconds in a reasonable time frame. Thus, one needs to go beyond first-principles simulations and use multiscale approaches to model the chemical-physical processes underlying graphene growth. Rearranging the atoms to synthesize graphene, C_{60} high-energy impacts on Cu and cage breaking are the first two steps towards graphene growth on the substrate. In particular, the energy released in the impact is absorbed by the distortion of the surface and dissipates via phonon excitations. The system quickly reaches a regime where excited-state dynamics is quenched and its evolution, thus, can be followed by methods based on the validity of the BO approximation, notably density functional theory (DFT).

Nevertheless, even if the computational cost of DFT calculations is much lower with respect to nonadiabatic molecular dynamics, the comparatively large time scale on which atomic rearrangement is expected to take place, typically of the order of seconds, is still prohibitive for first-principles simulations. In order to speed up the calculation, we thus use enhanced sampled techniques, such as metadynamics, or multiscale approaches, such as kinetic Monte Carlo (KMC) [50, 54]. In particular, we introduce a fictitious force coupled to a collective coordinate describing the number of carbon-carbon bonds that drives the system towards the formation of a carbon net, if clustering is energetically favourable. To carry out these calculations, we used the Vienna Ab initio Simulation Package (VASP) [55, 56]. Long-time metadynamics simulations provide a clear indication that the system, after cage rupture, tends to rearrange towards the formation of graphene. Furthermore, we were able to show that formation mechanisms are effective only above a critical carbon atom density on the surface, as shown in Fig. 5.10c.

Still, the time scale of graphene growth is much longer than can be modelled by metadynamics, in which electronic motion is explicitly included. Furthermore, by adopting this approach, we lose information on the actual time frame, as common in accelerated molecular dynamics methods. In this respect, the very long time scale dynamics, of the order of seconds, leading to graphene island formation and merging, is most effectively studied by means of KMC simulations [50]. Within this approach, nudged-elastic band simulations (NEB) using BO ground state DFT at RT are performed to calculate reaction activation energies and relevant transition rates (assuming Boltzmann-distributed occupation of the states) for carbon atom diffusion between adsorption sites on the copper surface, as well as the energy variation upon carbon-carbon bond formation. Once the rates and energies of all possible reactions and site jumps occurring on the copper surface are known, the KMC method is capable to follow the various stages leading to graphene production. Figure 5.10d shows the progressive creation and clustering of graphene flakes on the Cu surface after diffusion and merging of initially separated carbon atoms. This multiscale study pointed out the existence of a critical carbon density on the surface for successful graphene growth, in good agreement with our BO-DFT simulations of the early growth stages (see Fig. 5.10c) [50].

Finally, we notice that the kinetic energy threshold for projectile breaking can in principle be estimated also by a continuum mechanical model (CM) [57]. The kinetic energy threshold for projectile breaking in a CM is assumed proportional to the object volume V, where the proportionality constant is the product of the mechanical strength of the projectile and the ratio of the projectile and target densities. The threshold velocity for breakup at temperature T would then be given by:

$$\frac{1}{2}Mv^2 + \frac{1}{2}k_{\mathrm{B}}TnN = \frac{\rho_n}{\rho}\sigma_f V \tag{5.3}$$

where M is the mass of C_{60}, σ_f is the mechanical strength of the fullerene, ρ_n is its density, $\rho = 8960\,\mathrm{kg/m^3}$ is the copper density, $N = 60$ is the number of

atoms, $n = 3$ are the internal degrees of freedom per atom and k_B is the Boltzmann constant. Since in the SuMBE approach the rotational and vibrational degrees of freedom of C_{60} result frozen, the second term in the left-hand side of Eq. 5.3 can be neglected. Assuming σ_f of the order of the mechanical strength of carbon nanotubes [58] ($\simeq$50 GPa), the threshold kinetic energy of C_{60} breakup would be estimated $\simeq$40 eV. This value is in good agreement with our ab initio nonadiabatic simulations.

5.3 2D Carbon-Based Materials: Graphene and Its Low-Density Allotropes

The large interest expressed over the last decade in graphene, the bi-dimensional allotropic form of carbon, is largely determined by the honeycomb-shaped sp^2 carbon net from which it derives its unique electronic and mechanical properties [11, 12, 18, 47, 48, 59–65], such as unexpectedly high opacity for a thin atomic monolayer, high electron mobility at room temperature, with reported values in excess of 15,000 $cm^2\,V^{-1}\,s^{-1}$, and breaking strength over 100 times bigger than a hypothetical steel film of the same thickness [4]. Furthermore, pristine graphene differs from most three-dimensional materials being a semimetal or a zero-gap semiconductor, in which electrons and holes behave like Dirac fermions due to the linear dispersion in the vicinity of the six corners of the Brillouin zone, where valence and conduction bands touch upon.

Despite some concern raised about the stability of suspended monolayers owing to the theoretical prediction that a 2D lattice is unstable upon thermal fluctuations [66, 67], graphene was synthesized in 2004 by K. Novoselov and A. Geim [68], who managed to cleave out single-atom-thick crystallites from bulk graphite. Due to its properties, graphene finds application in a variety of fields, including electronic devices (transistors, sensors, batteries, transparent conductive coatings for solar cells, OLEDs, high frequency devices), nanocomposites (to make lighter aircraft, or embedded in plastics to conduct electricity, or again in sports equipment) or in medicine (such as in artificial cell membranes). Thus, despite the difficulties in synthesizing high-quality large-area graphene sheets [46, 49, 50], its great promises and achievements in the fields of materials science motivate the large scientific and technological efforts that the scientific community is pursuing.

Nevertheless, the importance of graphene goes beyond its own specific characteristics, as it represents the paradigm of a new class of bi-dimensional materials obtained from layered structures, such as transition metal dichalcogenides (TMDs) [69], silicene [70], germanene, the monolayer form of black phosphorous [71, 72] and boron nitride.

In this section, due to the large amount of reviews [4] and books [73] on the physics of graphene, we will only use graphene as a fundamental texture to deal with some novel carbon allotropes at lower density. In particular, we discuss the possibility to introduce interesting features in bi-dimensional all-carbon materials, keeping the planar structure and the sp^2-net of graphene. In this regard, one of the

most striking properties of graphene is its Young's modulus to density ratio, possibly the highest achieved so far. We discuss here a systematic method for finding novel energetically stable structures characterized by sp^2-hybridized carbon atoms with decreasing density but almost unchanged specific mechanical characteristics with respect to graphene. In this way, lower structural weight could be achieved which is an important request, e.g. in aerospace applications.

5.3.1 Structure Search Method

The geometry of graphene can be generated by using the two-dimensional packing of congruent discs touching each other in three points under the following constraints (for further details, see [74]):

- No two discs overlap;
- Each disc is in contact with at least another disc;
- For any choice of two discs in the packing, there is always a path connecting them through mutual contacts;
- Angles between the segments connecting two disc centres must be smaller than π rad (local stability);

With these constraints in place, one can search for novel structures with specific characteristics comparable to graphene and also for the least dense arrangement of discs in the plane which is an important issue on its own.

5.3.1.1 Graphene and Graphene Daughter

The packing of graphene, reproduced in the left-hand side of Fig. 5.12a, has a density equal to $\pi/(3\sqrt{3}) \sim 0.6046$ and can be used to create the graphene net, reported in the left panel of Fig. 5.12b, by positioning a carbon atom at the centre of each disc. One can generate a novel architecture by replacing each disc in the graphene packing with three discs having a radius $\frac{1}{1+2/\sqrt{3}}$ smaller than that of graphene, which leads to a less dense packing $\pi(7\sqrt{3}) - 12 \sim 0.390675$, as shown in the right panel of Fig. 5.12a. This process is known as "augmentation" [75], and the "*graphene daughter*" obtained by applying this procedure is reported in the right panel of Fig. 5.12b (called gr11 in [76]).

5.3.1.2 Tilene Parent and Tilene

By considering tilings with polygons having a number of sides larger than triangles, one can obtain the packing associated with, e.g. the square-octagon tiling. In the left panel of Fig. 5.13a, we show the tiling and in the left panel of Fig. 5.13b the

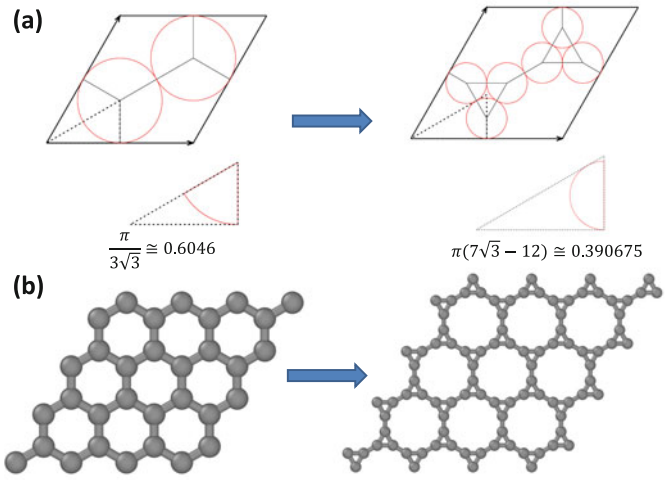

Fig. 5.12 (**a**) Graphene (left) and graphene daughter (right) unit cells. The latter can be obtained by using the two-dimensional packing of congruent discs, represented in the figure by red circles, touching each other. The centres of the nearest neighbour red discs, where carbon atoms lay, are connected by black lines representing the carbon bonds. (**b**) 4×4 supercells of graphene (left) and graphene daughter (right)

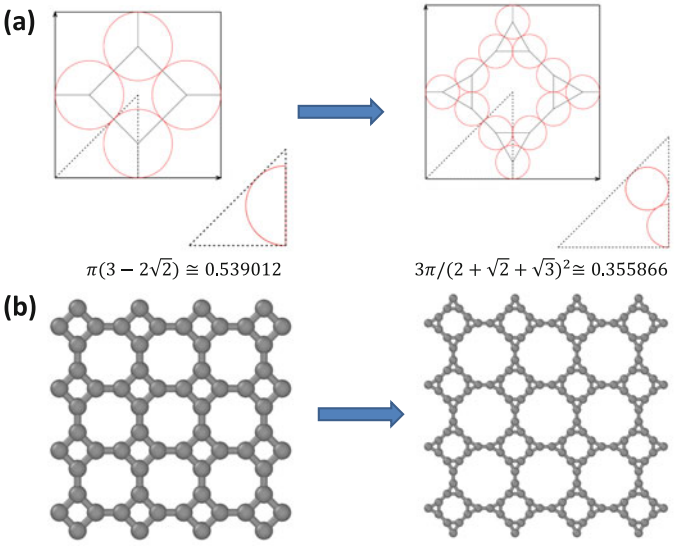

Fig. 5.13 (**a**) Tilene parent (left) and tilene (right) unit cells. The latter can be obtained by using the two-dimensional packing of congruent discs, represented in the figure by red circles, touching each other. The centres of the nearest neighbour red discs, where carbon atoms lay, are connected by black lines representing the carbon bonds. (**b**) 4×4 supercells of tilene parent (left) and tilene (right)

corresponding net of carbon atoms of "*tilene parent*" (octagraphene in [76]). Its packing factor is lower than graphene and equal to $\pi(3-2\sqrt{2}) \sim 0.539012$. Its augmentation, carried out under the constraints discussed in Sect. 5.3.1, leads to the lesser dense packing equal to $3\pi/(2+\sqrt{2}+\sqrt{3})^2 \sim 0.355866$ shown in the right panel of Fig. 5.13a. The resulting structure, called "*tilene*", is reported in the right panel of Fig. 5.13b.

5.3.1.3 Flakene Parent and Flakene

In the left panel of Fig. 5.14a, we report the trihexagonal tiling of the plane, obtained via regular polygons with the largest rings achieving a density equal to $\pi(2/\sqrt{3}-1) \sim 0.486006$. The resulting geometry filled with carbon atoms, called "*flakene parent*" (C_{64} graphenylene in [76]), is reported in the left panel of Fig. 5.14b. Its augmentation, shown in the right-hand side of Fig. 5.14a, shows a 24-sided polygon tiling with density equal to $3\sqrt{3}\pi/(20+3\sqrt{3}+6\sqrt{7}+2\sqrt{21}) \sim 0.324951$. The corresponding allotropic form, obtained by filling the discs at their centres by carbon atoms, is reported in the right panel of Fig. 5.14b, and we call it "*flakene*". We claim that the latter is one of the sp^2 structures with lowest density ever studied which agree to the locally jammed packing conditions.

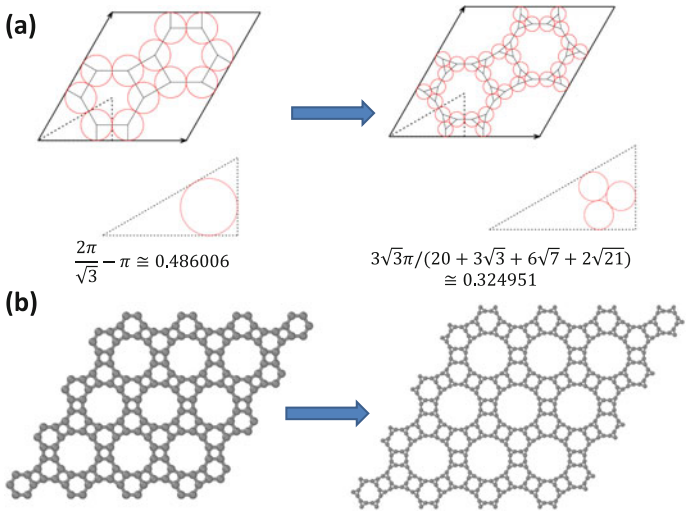

Fig. 5.14 (**a**) Flakene parent (left) and flakene (right) unit cells. The latter can be obtained by using the two-dimensional packing of congruent discs, represented in the figure by red circles, touching each other. The centres of the nearest neighbour red discs, where carbon atoms lay, are connected by black lines representing the carbon bonds. (**b**) 3×3 supercells of flakene parent (left) and flakene (right)

5.3.1.4 Liskene

Other carbon structures can be designed by relaxing the constraint of having only three-coordinated carbon atoms. A first example is given in Fig. 5.15a, b where we report the top and side views of pentagraphene [77], which has $four$ three-coordinated and two four-coordinated vertices. At variance with previous tilings, the plane is not filled using congruent discs, which reflects the fact that one cannot tile the plane by congruent pentagons. The resulting structure is not planar and is characterized by different bond lengths owing to the sp^2-sp^2 or sp^2-sp^3 hybridization. By applying the augmentation procedure to the pentagonal tiling, we obtain a planar three-coordinated structure that we name "*liskene*", which is shown in Fig. 5.16a. This daughter architecture is again a three-coordinated system with a density lower than the parent. In Fig. 5.16b we show the DFT optimized geometry of this geometrical tiling.

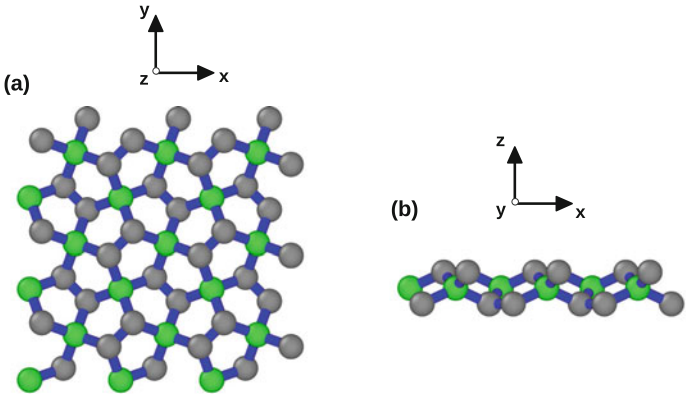

Fig. 5.15 (**a**) Top view of a 3×3 pentagraphene super cell; (**b**) side view of a 3×3 pentagraphene super cell. The sp^3-hybridized carbon atoms are reported in green colour, while in grey scale, we find the sp^2-hybridized carbon centres

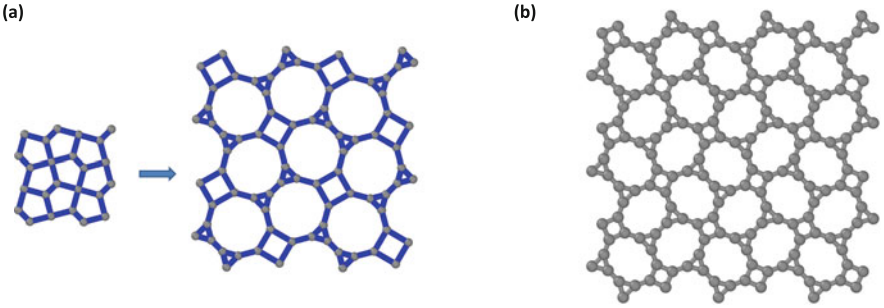

Fig. 5.16 (**a**) Augmentation of the Cairo pentagonal tiling. (**b**) 3×3 supercell of liskene after performing DFT minimization

5.3.2 Electronic Properties of 2D All-Carbon-Based Materials

Here we discuss the electronic band structure and the stress-strain characteristics of the father and daughter structures obtained by the space tiling and augmentation procedures previously introduced. Further details on computer simulations and methods can be found in Ref. [74].

In Table 5.1 we report the energy per atom and the cohesive energies. Graphene has a cohesive energy equal to 7.74 eV (experimental value is 7.6 eV [78, 79]) and still results the most energetically stable bi-dimensional allotrope of carbon. In general, with the notable exception of pentagraphene for which the out-of-plane geometry daughters into a planar sp^2 net, we observe that daughter architectures are characterized by lower stability along with lower density. While we notice that the loss of stability is not significant, as the energy difference between the less stable material (flakene) and graphene is of the order of 0.7%, the density is almost two times lower than that one of graphene (see the first column of Table 5.1).

Furthermore, we present the band structures alongside the relevant DOSs for the seven structural arrangements described in this section. Generally, we observe that moving from father to daughter in the case of graphene (Figs. 5.17 and 5.18), tilene (Figs. 5.19 and 5.20), flakene (Figs. 5.21 and 5.22) and pentagraphene (Figs. 5.23 and 5.24), a narrow band close to the Fermi level (reported as horizontal red lines in the figures) appears, increasing the metallic character of the parent structures. We argue that the appearance of an almost flat band can be the signature of geometrical and, thus, orbital frustration, similarly to the kagome lattice. These frustrated geometries pay the way also to the creation of strongly-correlated materials.

Table 5.1 First column: structure type. Second column: surface density. Third and fourth columns report the total energy per atom with respect to graphene and the cohesive energy per atom obtained upon structural optimization, respectively. With the exception of pentagraphene, all structures are planar, and each carbon atom is three-coordinated. In the table the following abbreviations were used: p. = parent, d. = daughter, dir. = direct gap, indir. = indirect gap

Structure	Density (atoms/Å^2)	Energy ([eV]/atom)	Cohesive energy ([eV]/atom)	Type	Bandgap [eV]
Graphene	0.379	0	7.7404	Semi-met.	0 (dir.)
Graphene d.	0.256	0.9882	6.7523	Metal	–
Tilene p.	0.336	0.5186	7.2219	Metal	–
Tilene	0.233	1.0765	6.6640	Metal	–
Flakene p.	0.301	0.6395	7.1009	Semi-met.	0.043 (dir.)
Flakene	0.212	1.1071	6.6334	Metal	–
Pentagraphene	0.452	0.9044	6.8361	Semicond	2.23 (ind.)
Liskene	0.297	0.7789	6.9615	Semicond	0.36 (ind.)
Liskene d.	0.247	1.0506	6.6897	Semicond	0.46 (ind.)

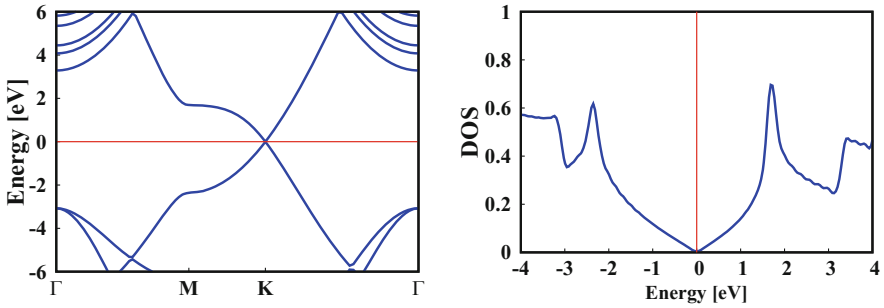

Fig. 5.17 Band structure (left) and DOS (right) of graphene. Fermi level is shifted to zero and reported as an horizontal red line in the left-hand side (bands) and as a vertical red line in the right-hand side (DOS) of the figure

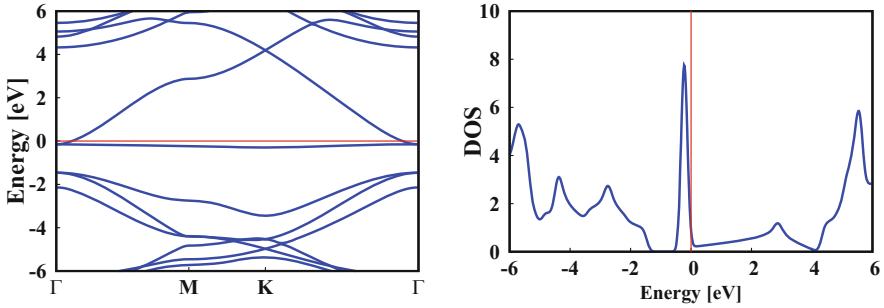

Fig. 5.18 Band structure and DOS of graphene daughter. Fermi level is shifted to zero and reported as a horizontal red line in the left-hand side (bands) and as a vertical red line in the right-hand side (DOS) of the figure

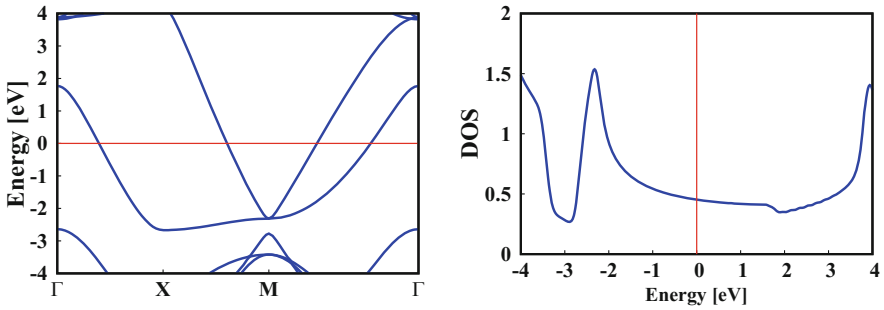

Fig. 5.19 Band structure and DOS of tilene parent. Fermi level is shifted to zero and reported as a horizontal red line in the left-hand side (bands) and as a vertical red line in the right-hand side (DOS) of the figure

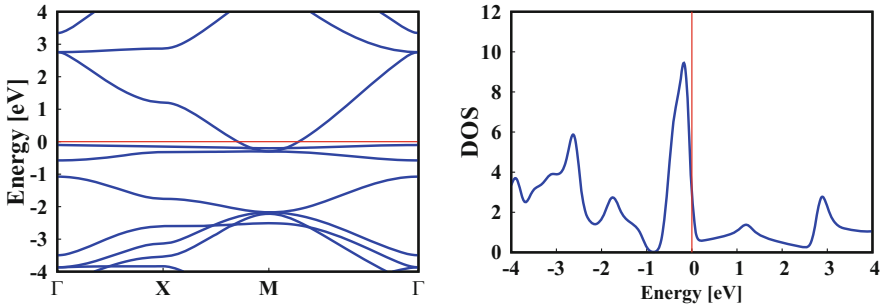

Fig. 5.20 Band structure and DOS of tilene. Fermi level is shifted to zero and reported as a horizontal red line in the left-hand side (bands) and as a vertical red line in the right-hand side (DOS) of the figure

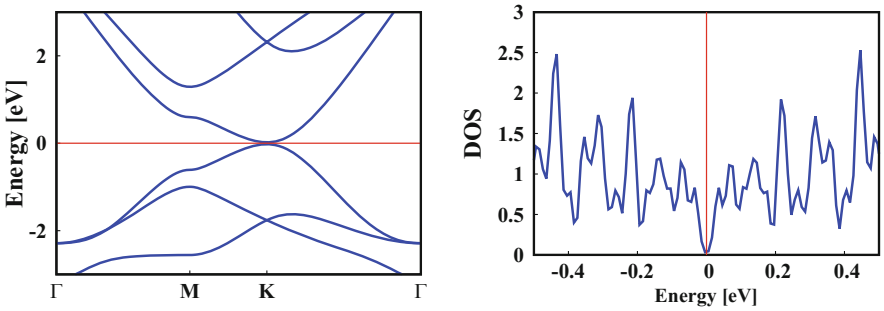

Fig. 5.21 Band structure and DOS of flakene parent. Fermi level is shifted to zero and reported as a horizontal red line in the left-hand side and as a vertical red line in the right-hand side of the figure. In this case we report for the DOS only the zoom near the Fermi energy which is obtained with a Fermi function smeared with a Gaussian of 0.0136 eV width in order to resolve the very low energy band gap

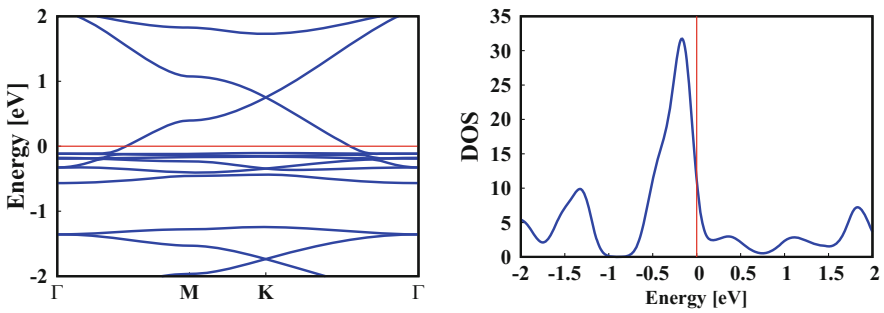

Fig. 5.22 Band structure and DOS of flakene. Fermi level is shifted to zero and reported as a horizontal red line in the left-hand side (bands) and as a vertical red line in the right-hand side (DOS) of the figure

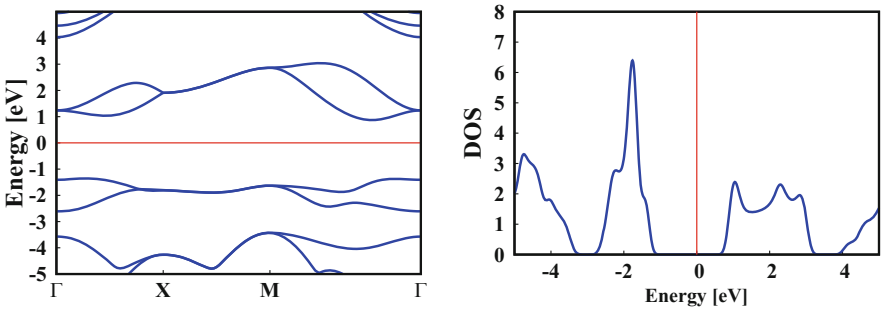

Fig. 5.23 Band structure and DOS of pentagraphene. Fermi level is shifted to zero and reported as a horizontal red line in the left-hand side (bands) and as a vertical red line in the right-hand side (DOS) of the figure

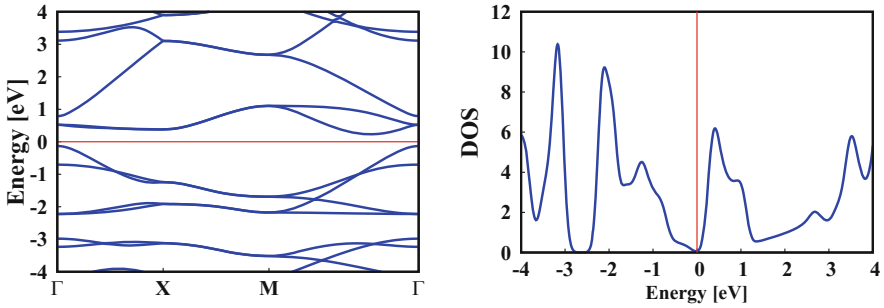

Fig. 5.24 Band structure and DOS of liskene. Fermi level is shifted to zero and reported as a horizontal red line in the left-hand side (bands) and as a vertical red line in the right-hand side (DOS) of the figure

5.3.3 *Mechanical Properties of Two-Dimensional All-Carbon Materials*

To assess the mechanical properties of the daughter and parent structures, one can carry out the ab initio simulations of the elastic stiffness tensor **C**, which in linear approximation represents the proportionality constants between stress and strain, $\boldsymbol{\sigma} = \boldsymbol{\varepsilon}\mathbf{C}$, where $\boldsymbol{\varepsilon}$ is the six-component strain vector and $\boldsymbol{\sigma}$ is the stress tensor. We remind in passing that the Hook's law may be written in tensor notation as $\sigma_i = C_{ij}\epsilon_j$ where $i, j = 1, \ldots, 6$ label the corresponding directions xx, yy, zz, yz, zx and xy, respectively. The first subscript identifies the direction in which the stress is measured, while the second one identifies the direction orthogonal to the plane on which the stress is acting. Since $\sigma_{ij} = \sigma_{ji}$ the independent stress components are six.

The elastic constants C_{ij} can be obtained as follows:

$$C_{ij} = \frac{\partial^2 F}{\partial \varepsilon_i \partial \varepsilon_j} \tag{5.4}$$

where in harmonic approximation (neglecting the thermal electronic contribution) the density function F can be expressed as:

$$F = F_0 + \frac{1}{2} F^{(2)} \varepsilon^2 + o(\varepsilon^3) \tag{5.5}$$

where F_0 and $1/2F^{(2)}\varepsilon^2$ are the static energy of the system and the lattice vibrational contribution, respectively. From the knowledge of the elastic constants, the Young's modulus E, which measures the material stiffness, and the Poisson's ratio ν, which measures the material tendency to expand perpendicularly to the direction of compression, can be computed as $E = (C_{11}^2 - C_{12}^2)/C_{11}$ and $\nu = C_{12}/C_{11}$, respectively.

In Table 5.2 we report the Poisson's ratio and the Young's modulus of all the 2D carbon allotropes discussed in this chapter with some other DFT values found in the literature [76, 80]. We remind that here we deal with two-dimensional structures where the specific mechanical properties should be referred to the area rather than the volume, at odds with the usual approach in 3D solids. Thus, ρ_A is the area density, and the quantities divided by ρ_A, such as E_A/ρ_A, must be understood per area density. The Young's modulus E, in particular, is a measure of the response to tensile or compressive loading and usually is measured in N/m^2 because the load is meant to be applied to an orthogonal cross section of the 3D solid. However, in 2D materials, such as graphene, the load is applied to a thin, in principle, monodimensional stripe because the orthogonal cross section of a two-dimensional solid is a line. Thus, the Young's modulus is measured as a force per unit length (N/m) rather than per unit area, and in order to distinguish this case from the 3D

Table 5.2 The columns report, respectively, the 1D (E_A) and 2D (E, thickness $t = 0.314$ nm) Young's modulus, Poisson's ratio (ν) and area-specific Young's modulus (E_A/ρ_A) of the parent and daughter carbon structures. To evaluate the accuracy of our simulations, we report a comparison with data in the literature where available. In the table the following abbreviations were used: p. = parent, d. = daughter

	E_A (N/m)	E (TPa)	ν	E_A/ρ_A (10^{-3} Nm kg^{-1})
Graphene	340	1.14	0.154	1.79
[76]	349		0.17	
Graphene d.	89.6	0.30	0.631	0.70
[76]	92.6		0.64	
Tilene p.	288	0.96	0.150	1.70
[80]	306		0.13	
Tilene	78.6	0.26	0.607	0.67
Flakene p.	205	0.69	0.263	1.36
[76]	210		0.27	
Flakene	38.6	0.13	0.746	0.36
Liskene	138	0.46	0.508	0.93
Liskene d.	93.1	0.31	0.517	0.75

case, we call it E_A. Of course one can define also the usual Young's modulus E by introducing a fictitious thickness t which for graphene is conventionally chosen equal to the intra-planar distance in solid graphite (0.335 nm). We also remind that at variance with a stable, isotropic, linear elastic 3D material where the bounds on Poisson's ratio are $-1 < \nu < 1/2$, for 2D materials, one can have $-1 < \nu < 1$ [81]. Furthermore, we notice that the Poisson's ratio of tilene, flakene and liskene shows that these materials are almost incompressible.

The most significant quantity to be compared with graphene is of course the specific modulus, that is, the Young's modulus divided by the mass density. In particular, dealing with a bi-dimensional material one can assess the Young's modulus E per area density ρ_A, E/ρ_A. We report this quantity in the last column of Table 5.2. We notice that graphene presents the biggest specific modulus among the materials studied here. Flakene, in particular, displays the lowest density among the investigated structures and shows a major drop in both the absolute and specific elastic moduli, which are from eight to five times lower than graphene. Nevertheless, while we do not find a material outperforming the specific properties of graphene in this respect and, thus, we do observe that the augmentation is only partially an advantageous route to follow in order to increase the specific modulus of graphene-like materials, the difference in the specific Young's modulus is less remarkable than for the absolute values, with the exception of flakene.

In Fig. 5.25 we report the specific biaxial modulus ($E_{bi} = C_{11} + C_{22}$) of the low-density carbon allotropes versus area density. The drop of flakene mechanical characteristics suggests that there is a threshold to the decrease of the density of these carbon-based planar materials, below which the mechanical properties are significantly depleted. Thus, the idea of decreasing the density, retaining the specific mechanical characteristics, can be pursued only to some extent at least as far as the Young's modulus is concerned.

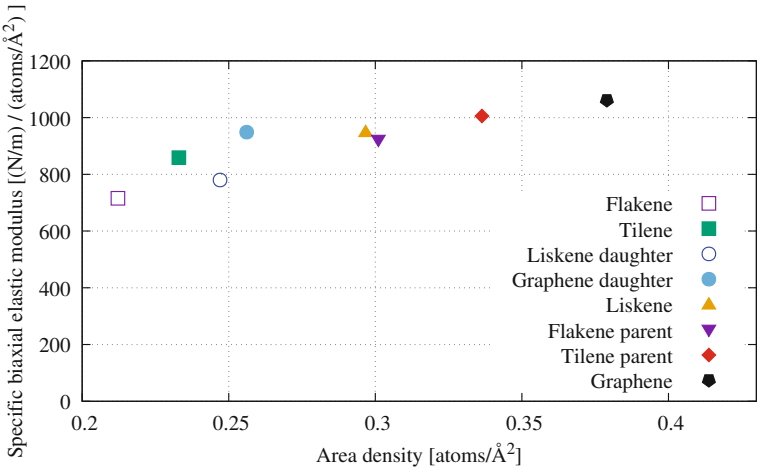

Fig. 5.25 Specific biaxial elastic modulus versus area. (Adapted from Ref. [74])

Further information on the mechanical properties of the graphene-based low-density structures can be obtained by analysing the stress-strain curves from which several quantities can be obtained, such as the absolute fracture strain, tensile strength and toughness.

In Fig. 5.26 we plot the stress-strain curves of these parent and daughter structures along the Cartesian directions x, y, which represent the zig-zag and armchair directions of graphene ribbon, or along the 45° direction owing to the unit cell symmetry of tilene and liskene. The stress-strain characteristics show (i)

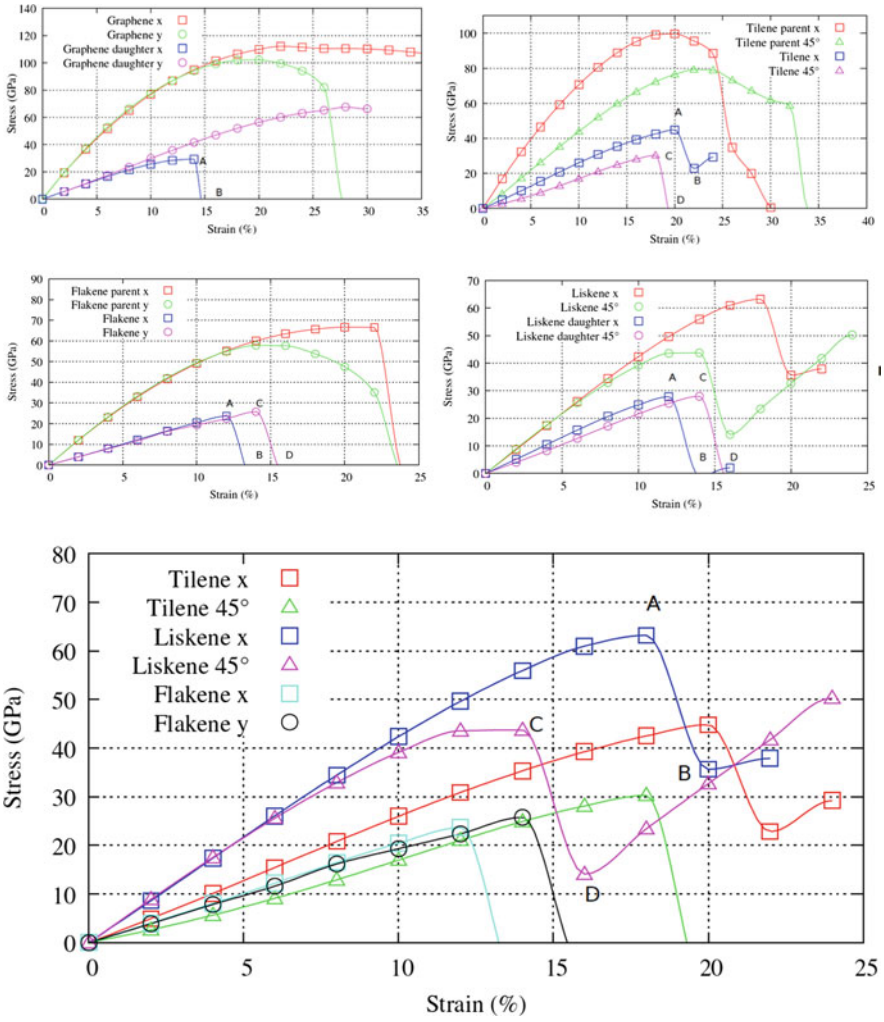

Fig. 5.26 Stress-strain curves of parent and daughter structures along the x-direction (or zig-zag), the y-direction (or armchair) and 45° (diagonal). The differently coloured lines represent the best fits to the ab initio data. (Adapted from Ref. [74])

the anisotropic response of these structures under uniaxial loading along different directions, which results in a nonlinear, hyperelastic constitutive equation; (ii) the significant depletion of the absolute mechanical response from parent to daughter architectures, with a strong decrement in toughness, yield and ultimate strengths (see also Table 5.3); and (iii) that the mechanical response is basically determined by the reaction of triangular (tougher) or square (softer) shapes in the structures.

As a final remark, we point out that the picture so far described concerning the absolute values slightly changes when we look at the specific properties reported in the last two columns of Table 5.3. Indeed, the specific ultimate strength of our novel 2D structures is comparable to graphene or even higher than the latter in the case of the tilene parent. Nevertheless, the trend of the specific toughness, which measures the ability of a material to absorb energy before fracture, is overwhelmingly favourable to graphene with respect to the other structures.

Table 5.3 Fracture strain (first column), strength (second column), strength $\times t$ (third column) and toughness$\times t$ (fourth column) of the parent and daughter planar structures alongside the specific strength and specific toughness (fifth and sixth columns). The conventional thickness of the graphenic materials is considered to be $t = 3.35$ Å. In the table the following abbreviations were used: p. = parent, d. = daughter

	Loading direction	Fracture strain (%)	Strength (GPa)	Strength $\times t$ (N/m)	Toughness $\times t$ ($J\,m^{-2}$)	Specific strength ($MNm\,kg^{-1}$)	Specific toughness ($MJ\,kg^{-1}$)
Graphene	x	>35	112	37.5	>9.83	49.7	> 13.0
	y	26–28	102	34.2	6.51	45.2	8.61
Graphene d.	x	18–20	29.3	9.81	0.83	19.2	1.62
	y	>30	67.7	22.6	>3.63	44.3	> 7.11
Tilene p.	x,y	24–26	99.6	33.4	5.55	49.7	8.27
	45°	32–34	79.1	26.5	5.68	39.5	8.47
Tilene	x,y	20–22	44.8	15.0	1.66	32.3	3.57
	45°	18–20	30.3	10.2	0.92	21.9	1.97
Flakene p.	x	22–24	66.7	22.3	3.37	37.2	5.61
	y	22–24	57.9	19.4	3.01	32.3	5.02
Flakene	x	12–14	23.6	7.92	0.49	18.7	1.16
	y	14–16	25.8	8.63	0.63	20.4	1.49
Liskene	x,y	18–20	63.2	21.2	2.19	35.8	3.70
	45°	14–16	43.8	14.7	1.27	24.7	2.14
Liskene d.	x,y	12–14	27.8	9.32	0.59	18.5	1.20
	45°	14–16	28.0	9.37	0.68	19.0	1.37

5.4 Graphene Pseudospheres

Graphene is a versatile material, which can be arranged in the shape of stripes (nanoribbons), rolled nanotubes or piled up in the direction orthogonal to its plane (graphite). So, it is a legitimate thinking to search for other shapes.

In this respect, Beltrami's pseudosphere, named after the Italian mathematician Eugenio Beltrami who first devised this hyperbolic shape, is a surface of revolution characterized by constant negative Gaussian curvature. Thus, it represents the negative counterpart of the sphere which, at odds, is characterized by constant positive curvature. A Beltrami's pseudosphere can be realized by using carbon (see Fig. 5.27) [82] and represents a portion of the Lobachevsky geometry on a real surface. Its counterpart can be also realized using carbon and is represented by the previously discussed fullerene shape.

Graphene pseudospheres are carbon-based energetically stable molecular structures, which (i) correspond to a non-Euclidean crystallographic group, namely, a loxodromic subgroup of $SL\,(2,\mathbb{Z})$, and (ii) have an unavoidable singular boundary, where planar graphene meets the "trumpet" (see Fig. 5.27).

We devise that owing to its unique electronic properties, a graphene monolayer arranged in a pseudosphere shape can be used to realize a realistic analogue of a quantum field in a curved space-time and thus can be used to test certain scenarios of the physics of curved space-times, e.g. the Hawking-Unruh effect [83]. The latter states that the ground state of an inertial observer is seen in thermodynamic equilibrium with a nonzero temperature by a uniformly accelerating observer. Thus,

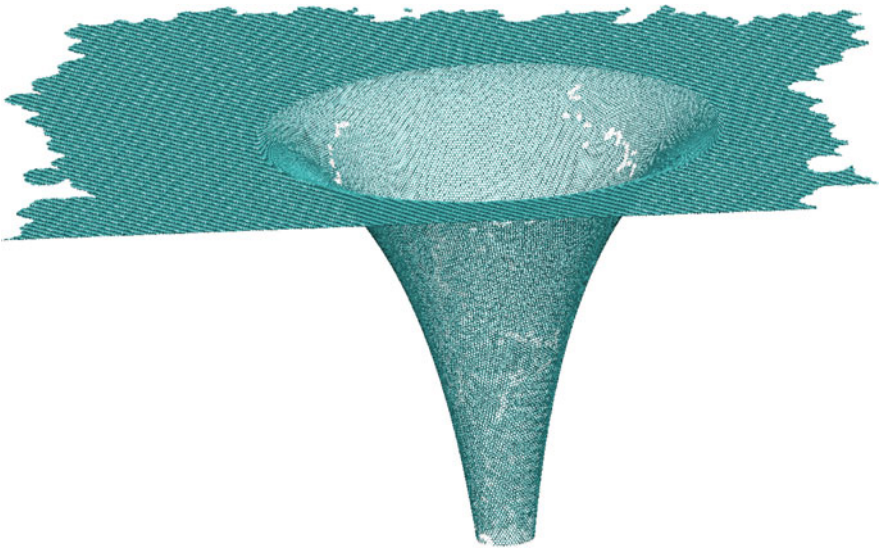

Fig. 5.27 A graphene pseudosphere

a quantum fields in a space-time with a horizon should exhibit a thermal character. This effect is closely related to the local density of states (LDOS) of the graphene pseudosphere, which could be possibly considered as a black hole analogue. Indeed, one can show that by solving the Dirac equation in a continuum space-time, the LDOS has the following analytic behaviour [83]:

$$\rho(E,u,r) = \frac{1}{(\hbar v_F)^2} \frac{\exp^{(-2u/r)}}{\exp^{E/(k_B T_0 \exp^{u/r})} - 1} \tag{5.6}$$

where $T_0 = (\hbar v_F)^2 \exp^{u/r} \rho(0,u,r)$ defines the Hawking temperature, u is the hyperbolic coordinate along the pseudosphere axis, k_B is the Boltzmann constant, v_F is the Fermi energy and r is the pseudosphere maximum radius (event horizon). We remind that the Hawking temperature is the temperature to which black holes, acting as perfect blackbodies, radiate. The electromagnetic radiation, owing to quantum effects, is emitted at a temperature inversely proportional to the mass of the black hole. Only electrons with an energy $E = \hbar v_F / r$, which represents the intrinsic energy scale associated to the pseudosphere, have a long enough wavelength to experience the whole curved surface; hence their contribution to the LDOS is important. We notice that for a graphene pseudosphere with a radius $r = 0.1\,\mu\text{m}$, the Hawking temperature is about 13 K.

5.5 1D Carbon-Based Materials

Carbon nanotubes (CNTs) are graphitic sheets rolled in hollow cylinders with walls made by hexagonal carbon rings (see Fig. 5.4). They often form large bundles and are capped by domed structures at their termination. Two types of CNTs have been synthesized: single-wall carbon nanotubes (SWCNTs or simply CNTs), consisting of a single rolled layer of graphene, and multiwall carbon nanotubes (MWCNTs), made by multiple graphene layers telescoped about one another. CNTs were first isolated and characterized by Iijima in 1991 [8].

CNTs inherit from graphene some of its unique physical and chemical properties, such as structural rigidity, flexibility, strength, and ideal thermal conductivity. Owing to these intrinsic features, 1D all-carbon nanomaterials found a wide variety of applications in molecular electronics and in semiconducting device technologies, such as FET, electrodes, power cables, fibres, composites, actuators, sensors and biosensors [6]. Furthermore, due to their small size and biocompatibility, CNTs express great potential in the emerging field of nanomedicine, e.g. for implantable applications for continuous monitoring of clinically relevant analytes, including glucose, or in food industry and environmental sciences. Finally, due their hollow, curved shape and the large surface/volume ratio, CNTs can be easily doped and functionalized, e.g. using carboxyl (COOH) and/or hydroxyl (OH) groups, to acquire the desired electronic, optical or adsorption properties. At odds with

graphene, however, the electronic properties of single CNTs depend on their chirality. The nanotube chirality is defined by the specific and discrete chiral angles at which graphene sheets are rolled. In particular, the chirality is identified by a couple of numbers (n, m), which define a vector $(C_h = na_1 + ma_2)$ in an infinite graphene sheet that describes how to "roll up" the graphene sheet to make the nanotube. The nanotube diameter $(d = (n^2 + m^2 + nm)^{1/2})$, its density, lattice structure and the electronic characteristics, such as the conductance, depend only on the chirality indexes (n, m). A SWNT is considered metallic, with conductivity showing rectification or ohmic characteristics, if the fraction $(n - m)/3$ is an integer value. Otherwise, the nanotube is semiconducting, with variable energy gaps ranging from a few meV to a few tenths of an eV. In this section we will investigate the electronic properties of small semiconductor CNTs using high-level accuracy many-body perturbation theory. In particular, we use the GW approximation, which assumes that the self-energy of a many-body electron system can be assessed by keeping only the lowest order term in the expansion of the self-energy in powers of the screened interaction W. By doing so the self-energy is written as the product of G, the one-body Green's function, and W, the screened Coulomb interaction [84].

5.5.1 The GW Method for CNTs

Recently, Umari and coworkers have developed a method for performing accurate and well-converged GW calculations in large simulation cells based on reduced basis sets for expressing the polarizability operators [85] and on Lanczos's chains for avoiding sums over unoccupied one-particle states [86]. This scheme, which will be revised in this section, was used for investigating the dependence of electronic band gaps with respect to the tube diameter for a number of semiconducting single-wall zig-zag CNTs, with diameters ranging from 0.56 to 1.27 nm [11, 12].

Beyond the independent electron approximation, the electronic states in a strongly interacting system can be described through a quasi-particle picture in which the behaviour of the bare electron is strongly renormalized by the presence of the other electrons of the system. On the experimental side, this quasi-particle behaviour can be probed via direct and inverse photoelectron spectroscopy. On the theoretical side, MBPT and, in particular, the G_0W_0 approximation [87] represent a rather simple, though accurate approach for addressing quasi-particle calculations on large systems. The G_0W_0 approach allows one to apply many-body perturbative corrections to a starting DFT calculation. Within this method, the quasi-particle energy level E_i for the i-th Kohn-Sham state is obtained from the solution of the following self-consistent one-variable equation:

$$E_i = \epsilon_i + \langle \psi_i | \, \Sigma_c \left(E_i \right) | \psi_i \rangle - \langle \psi_i | \, V_{xc} \, | \psi_i \rangle + \langle \psi_i | \, \Sigma_x \, | \psi_i \rangle \, , \tag{5.7}$$

where ψ_i is the i-th Kohn-Sham eigenstate, ϵ_i the eigenenergy, V_{xc} is the exchange and correlation potential and Σ_c and Σ_x are the correlation and exchange parts

of the self-energy operator, respectively. In this approach, Σ_c is found from the convolution of the one-body Green's function G_0, obtained from DFT calculations, with the correlation part of the screened Coulomb potential W_0^c, obtained at random-phase approximation level (RPA [84]):

$$\Sigma_c\left(\mathbf{r}, \mathbf{r}'; \omega\right) = \frac{1}{2\pi} \int d\omega' G_0\left(\mathbf{r}, \mathbf{r}'; \omega + \omega'\right) W_0^c\left(\mathbf{r}, \mathbf{r}'; \omega'\right). \tag{5.8}$$

Despite the apparent simplicity of this approach, its application requires a considerably larger effort than the starting DFT calculation. In fact, the evaluation of operators, such as G_0 and W_0^c, at many frequencies contains the sum over a large (in principle infinite) number of unoccupied Kohn-Sham states, resulting in a convergency very difficult to be achieved [88]. The approach developed by Umari et al. overcomes these drawbacks by expanding the polarizability and the screened Coulomb interaction operators through a reduced (optimal) basis set [85], which allows us to obtain overall good accuracy. Furthermore, within this method we avoid the sum over unoccupied states by a Lanczos' chains approach [86].

5.5.2 *Band Gap of Model CNTs*

Here, we show the application of this method to the calculations of the electronic band gap of a selected number of semiconducting single-wall zig-zag CNT with chirality indices equal to (7,0), (8,0), (10,0), (11,0), (13,0) (14,0), (16,0). Computational details can be found in Ref. [11], while here we summarize the main results. DFT calculations were performed within the local-density approximation (LDA) [89] using norm-conserving pseudopotentials with single-particle orbitals and charge densities expanded in plane waves. The calculations of the electronic band gaps of the selected CNTs neglect the excitonic effects due to the electron-hole pair formation. Within this approximation, the electronic band gap, usually indicated as E_{11}, corresponds to the energy difference relative to the van Hove singularities appearing in the density of electronic states below and above the Fermi level. The energy difference relative to the gap between the second singularities above and below the Fermi level is referred to as E_{22} (see top panel of Fig. 5.28). However, we remember that experimental measurements of the band gap performed through optical spectroscopies record fluorescence lines that include the correlated motion of electrons and holes, which affects strongly the spectrum. Indeed, in a semiconductor, where excitonic effects are not negligible, the exciton binding energy E_b strongly renormalizes the "electronic or fundamental band gap" E_g, that is, $E_{opt} = E_g - E_b$. Thus, there is a distinction between the optical band gap, which represents the threshold value for photons to be absorbed, and the "electronic or fundamental band gap", which represents the threshold value for creating an electron-hole pair that is not bound together. Therefore, experimental band gaps are dramatically renormalized by this effect and one rather measures

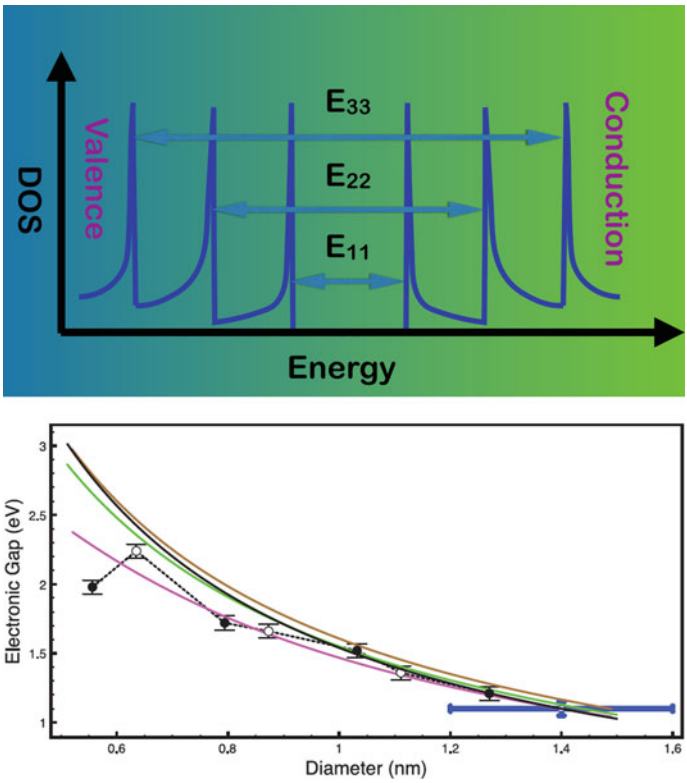

Fig. 5.28 Top panel: scheme of the electronic transitions in semiconductor CNTs. Bottom: electronic band gaps for semiconducting CNT of diameter d_t, corresponding to optical transitions. Full black circles: GW results for mod1 zig-zag CNT. White circles: GW results for mod2 zig-zag CNT. The error bars refer to the total estimated accuracy of the GW energy levels with the dashed black line guiding the eye. Black line: fit of GW results for large CNT (see text). Theoretical estimates for semiconducting CNT as by: Eqs. 5.9 (green line), 5.10, and 5.11 for zig-zag CNT of mod1 (purple line) and mod2 (brown line) species. The experimental STS measurement of Ref. [91] is reported together with error bars (blue line). (Adapted from Ref. [11])

the energies of the lowest (E_{1A_2}) and of the second lowest (E_{2A_1}) optically active exciton states and their difference. We remind that E_{1A_2}, E_{2A_1} label the excitonic states by $n\Gamma$, where $n-1$ is the number of nodes in the hydrogenic function that represents the exciton and provides a physically grounded guess to the ordering in which the different exciton states might appear (higher n corresponds to higher excitonic states), and Γ labels its irreducible representation. For example A_1 is the totally symmetric representation of the symmetry group of the chiral nanotubes [90]. Moreover, in some specific zig-zag small diameter CNTs, such as the (7,0) and (8,0) CNTs, the band gap corresponding to the optically active excitons may be even energetically higher than the minimum energy semiconducting band gap. As such, the experimental values of the electronic band gap do not match the calculated ones.

In principle, scanning tunneling spectroscopy (STS) could give a direct measure of electronic band gaps. However, in such a case screening effects arising from the metal substrate on which the CNT is dispersed become important. A model of these screening effects was tried, but the final error bars are quite large [91]. Therefore, accessing to electronic band gaps usually relies both on optical measurement and theoretical modelling.

The edges for fluorescence emission have been measured for several CNTs, and the dependence on the tube diameter has been fitted with model functions [92, 93]. For example, Dukovic et al. [93] reports the following behaviour for the optical first emission gap E_{op}^{11}:

$$E_{\text{op}}^{11} = \frac{1.11}{d_t + 0.11}\text{eV} \tag{5.9}$$

where the diameter d_t is expressed in nm. A further formula relating the electronic gap vs. CNT diameter is obtained by Weisman and Bachilo [92] as follows:

$$\begin{aligned} E_{\text{op}}^{11}(\text{mod1}) &= \frac{1.241 * 10^3\,\text{eV}}{157.5 + 1066.9 d_t} - \frac{0.0957\,[\cos(3\alpha)]^{1.374}}{d_t^{2.272}} \\ E_{\text{op}}^{11}(\text{mod2}) &= \frac{1.241 * 10^3\,\text{eV}}{157.5 + 1066.9 d_t} + \frac{0.04307\,[\cos(3\alpha)]^{0.886}}{d_t^{2.129}} \end{aligned} \tag{5.10}$$

where α is the chiral angle [94] and $mod(n - m, 3) = 1$ (mod1 species, such as the (7,0), (10,0), (13,0) and (16,0) CNTs) or $mod(n - m, 3) = 2$ (mod2 species, such as the (8,0), (11,0) and (14,0) CNTs). For zig-zag CNTs one has $\alpha = 0$.

By solving a model electron-hole Hamiltonian [95], which delivers exciton binding energies in agreement with accurate GW-Bethe-Salpeter calculations [96], the semiconducting CNT binding energy $E_{1A_2}^{\text{bind}}$ for the lowest $1A_2$ exciton can be expressed as:

$$E_{1A_2}^{\text{bind}} \approx \frac{0.55}{d_t}\text{eV} \tag{5.11}$$

The electronic band gap E^{11} can thus be obtained by Eqs. 5.10 and 5.11 as:

$$E^{11} = E_{\text{op}}^{11} + E_{1A_2}^{\text{bind}} \tag{5.12}$$

In Table 5.4 we report the calculated band gaps relative to optically allowed electronic transitions for the CNTs under investigation. In the (7,0) and (8,0) CNTs, the fundamental electronic band gap refers to transitions that are not optically allowed. We note that our calculated value of the fundamental gap for the (8,0) CNT, equal to 1.80 eV, is in good agreement with previous GW calculations from Spataru and coworkers [10] giving 1.75 eV and from Kang et al. [97] giving 1.51 eV. The calculated gap for the (8,0) CNT relative to optically allowed transitions (2.24 eV)

Table 5.4 Electronic band gaps from LDA and GW calculations for the semiconducting zig-zag CNTs under investigation with chirality indices (m,n) (first column). The gaps are relative to optically allowed transitions. When the electronic band gap for optically allowed transitions differs from the fundamental electronic band gap, we have reported also the latter in parenthesis

(m,n)	LDA (eV)	GW(eV)
(7,0)	0.16	1.98 (1.47)
(8,0)	0.5	2.24 (1.80)
(10,0)	0.80	1.72
(11,0)	0.95	1.66
(13,0)	0.65	1.52
(14,0)	0.74	1.36
(16,0)	0.56	1.21

is in good agreement with the value of 2.54 eV from Spataru et al. [10] and with the value of 2.14 eV previously found by Taioli et al. with a preliminary version of the method here used [12].

Furthermore, our calculated value of the fundamental electronic gap for the (7,0) CNT is 1.47 eV, which is higher than the value of 0.60 eV reported in a previous study by Miyake et al. [98] and the value of 1.22 eV obtained by Taioli et al. [12]. The latter values are reported for the case of zig-zag semiconducting CNT for both mod1 and mod2 species. We note that a good agreement of our calculated GW electronic gaps with the previous estimates is found for the investigated diameter sizes, excluding the (7,0) CNT. In this case, curvature effects due to the small size of the CNT become important and σ and π states mix into hybrids with partly sp^2 and sp^3 character. It should be noted that LDA results, not reported in this figure, are far from the theoretical/experimental lines as one can see in Table 5.4. The GW results for the largest CNTs are also in excellent agreement with the STS measurement of the electronic gap by Lin et al. [91] for the case of 1.4 nm diameter CNT.

Nevertheless, CNTs used in electronic devices have of course diameters larger than those studied here. It is thus interesting to extrapolate our GW results to obtain a model electronic gap-diameter function. To this goal, we fitted our GW results for CNT larger than 1.0 nm with the simple relation $E^{11} = \frac{a}{d_t}$ pointing towards a closed gap in the large diameter limit as expected from zero-gap graphene. We find a value $a = 1.54\,\text{eV}\times\,\text{nm}$.

5.6 3D Carbon-Based Structures

As a last step into the "dimensional ladder", we finally discuss a number of properties of all-carbon 3D architectures, notably the charge transport in diamond and graphite, and the mechanical and thermal properties of carbon foams.

5.6.1 Two Case Studies: Transport Properties of Diamond and Graphite

First we consider the electron transport properties from reflection electron energy-loss spectroscopy (REELS) measurements of diamond and graphite films. Indeed, while graphene and other 2D materials are considered the most promising replacements of silicon in future electronics [99], difficulties in finding scalable, cheap and safe techniques to grow high-quality graphene sheets currently hamper the hypothetical potential of this 2D material. Furthermore, in order to use graphene in microelectronic applications, a band gap must be opened [47, 48]. In this regard, other naturally occurring allotropic forms of carbon, such as diamond and graphite, could be used as viable candidates for an all-carbon electronics.

For example, diamond, owing to several ideal characteristics, such as large thermal conductivity, high charge mobility, wide band gap, optical isotropic structure and robustness, can be considered also a competitor in the carbon-based revolution for enhancing the performances of electronic devices. On the other side, graphite is the most stable naturally occurring carbon allotrope, characterized by a layered architecture with both strong in-plane sp^2-bonds, comparable in cohesive energy to those found in diamond, and weak interplanar bonds that make it soft and malleable as well as anisotropic to external perturbations. Furthermore, graphite shows optimal heat, large electrical conductivity and high strength and stiffness even above 3000 °C.

5.6.1.1 The Dielectric Response of Materials

The study of charge transport in solids is of paramount importance in several applications, ranging from materials characterization via electron microscopy and spectroscopy to the production of optimally designed electronic devices by controlling the energy transfer scattering processes that occur in different energy ranges [100–102].

In this regard, we notice that the analysis of the collision events taking place within a solid is based on the accurate assessment of the frequency-dependent dielectric function, which links microscopic properties, such as the band structure of solids, to macroscopic features that are the direct outcome of spectroscopic experiments, such as the absorption coefficient, the surface impedance or the electron energy loss. Indeed, the dielectric function $\epsilon(W, q)$, where W is the energy loss and q the transferred momentum, provides access to the full electronic excitation spectrum of the material in both energy and momentum space. Furthermore, we observe that the dielectric function is the only material property necessary to assess the inelastic cross sections. In particular, the real part of the dielectric function $\Re[\epsilon]$ describes the screening (i.e. the polarizability) of the medium, while the imaginary part $\Im[\epsilon]$ the absorption. In general, single-electron excitations, such as excitons, interband excitations and core-hole ionizations, are connected to the maxima of

$\epsilon(W, q)$, while collective many-electron excitations (plasmons), which are typical of the condensed phase, are related to the minima of $\epsilon(W, q)$, which usually appear if the two conditions $\Im[\epsilon(W, q)] \ll 1$ and $\Re[\epsilon(W, q)] = 0$ occur. From the knowledge of $\epsilon(W, q)$, one can calculate observables of paramount importance for designing novel optical and electronic devices, such as inelastic mean free path, stopping power, plasmons and secondary electron spectra.

To compute the dielectric function dependence on the energy and transferred momentum, one can proceed along three different routes [18]. First, one may use a semiclassical approach, whereby one assumes the knowledge of the long wavelength or optical limit of the dielectric function ($q \rightarrow 0$); this information is usually provided by experimental measurements of optical absorption [103], transmission electron energy-loss experiments [104, 105] or ab initio simulations [106]. To go beyond the optical limit, one can extend the dielectric response to finite momenta by using a Drude-Lotentz (DL) model. In this approach, the dielectric function is approximated by a number of damped harmonic oscillators with frequencies equal to the plasmon frequencies obtained by fitting experimental data [107, 108] and a friction-type force to simulate general dissipative processes; this extension of the dielectric response to finite momenta with the DL functions represents the most accurate approach available [109]. The second viable approach concerns the ab initio calculation of the dielectric response for vanishing momentum transfer and then its extension to finite momenta by a DL model. Finally, one could assess the dispersion law of the dielectric function at finite momentum q by using a full ab initio (AI) approach, based on time-dependent density functional simulations [110] in the linear-response regime (LR-TDDFT) [111–113].

The so-derived dielectric functions are used as input for a Monte Carlo description of the inelastic scattering probability to calculate the energy loss of electrons along their path within the solid. The comparison between our simulated and recorded REELS allows us to assess the impact that external tuneable parameters and semiclassical assumptions might have on the accuracy of simulated spectral line shapes for the characterization of 3D carbon-based materials.

Frequency- and Momentum-Dependent Dielectric Function

The microscopic representation of electromagnetic fields in interaction with periodic crystals can be described in terms of the microscopic dielectric function $\epsilon_{\mathbf{G},\mathbf{G}'}(\mathbf{q}, W) = \epsilon(\mathbf{q} + \mathbf{G}, \mathbf{q} + \mathbf{G}', W)$, where $\mathbf{G}$ and $\mathbf{G}'$ are the lattice vectors in the reciprocal space, while $\mathbf{q}$ is the transferred momentum contained in the first Brillouin zone. The relation between the latter quantity, which is usually the outcome of ab initio simulations, and the experimentally measurable macroscopic dielectric function is the following [114, 115]:

$$\epsilon(\mathbf{q}, W) = \left[\epsilon^{-1}_{\mathbf{G}=0,\mathbf{G}'=0}(\mathbf{q}, W)\right]^{-1} \tag{5.13}$$

where the $G = G' = 0$ limit results in an average over the unit cell of the corresponding microscopic quantity, which can exhibit rapid oscillations at the atomic level.

The dielectric function provides access to the differential inelastic scattering cross section σ_{inel}, since [116]:

$$\frac{d\sigma_{\text{inel}}}{dW} = \frac{1}{\rho\pi a_0 T}\int_{q_-}^{q_+}\frac{dq}{q}\text{Im}\left[-\frac{1}{\epsilon(q,W)}\right] \tag{5.14}$$

where a_0 is the Bohr radius, ρ the atomic density of the target material, q is the transferred momentum and the integration limits are $q_- = \sqrt{2m}(\sqrt{T} - \sqrt{T-W})$ and $q_+ = \sqrt{2m}(\sqrt{T} + \sqrt{T-W})$. Equation 5.14 states that at a given incident electron energy and scattering angle, the negative inverse of the imaginary part of the dielectric function is the electron energy loss in a transmission experiment, which is defined as follows:

$$\text{ELF} = \text{Im}\left[-\frac{1}{\epsilon(\mathbf{q},W)}\right] \tag{5.15}$$

This quantity is called the energy-loss function (ELF) and depends only on the material specific properties. At variance, the inelastic scattering cross section is also a function of the incident electron beam kinetic energy. Finally, the total electron mean free path λ is given by [117]:

$$\lambda = \frac{1}{\rho(\sigma_{\text{el}} + \sigma_{\text{inel}})} \tag{5.16}$$

where σ_{inel} is the total inelastic mean free path, obtained by integrating Eq. 5.14 over the energy range, and σ_{el} is the elastic scattering cross section. In general, the momentum transferred by electrons upon collision is neither negligible nor constant in different energy ranges, and the material dispersion relation (E vs. $\mathbf{q}$) shows generally a non-flat behaviour. Thus, one needs to evaluate the dielectric function also out of the optical limit before calculating the expression in Eq. 5.15.

First, we notice that Eq. 5.15 is obtained under the assumptions of validity of the first-order Born approximation, which works for sufficiently fast, point-like, particles weakly deflected by potential scattering. These requirements turn out to be met when the incident particle kinetic energy is $T\,(\text{eV}) \gg 13.6Z^2 \simeq 490\,\text{eV}$, which is the typical situation of valence electrons [118]. Nevertheless, we will show applications of Eq. 5.15 also to slow (up to a few tens of eV) secondary electron emission.

Second, we observe that to invert the dielectric matrix in Eq. 5.15, one needs also to assess the dependence on finite momentum transfer $\mathbf{q}$. In this regard, we now revise the two different approaches that have been devised to this purpose; these are the DL and the full AI models.

Drude-Lorentz Model

Within the DL model, the material response to an applied uniform external electromagnetic field is approximated by considering the target screening electrons as harmonic oscillators of frequency $\omega_n = \frac{E_n}{\hbar}$, where E_n is the plasmon energy. Charge oscillations are damped via a damping term Γ_n, which introduces friction-like forces affecting the oscillatory harmonic motion.

Outside the optical domain, the ELF is extrapolated to nonvanishing momenta by using a quadratic dispersion law [109, 118, 119], which basically assumes that the valence electrons in the solid can be considered as a noninteracting homogeneous gas. The plasmon energy is expanded to second order in q as follows:

$$E_n(q \neq 0) = E_n(q = 0) + \frac{\hbar^2 q^2}{2m} \tag{5.17}$$

The ELF is finally expressed as a sum over all oscillators of q-dependent generalized DL functions with a full-width-half-maximum Γ_n [118, 120, 121]:

$$\mathrm{Im}\left[-\frac{1}{\epsilon(q, W)}\right] = \sum_n \frac{A_n \Gamma_n W}{(E_n^2(q) - W^2)^2 - (\Gamma_n W)^2} \tag{5.18}$$

where A_n is the oscillator strength of the nth-oscillator which are obtained by fitting procedures of optical data. We remind that the f-sum rule must be exactly satisfied by the Drude dielectric function [122].

Ab Initio Simulations

The dielectric function of materials can be also obtained from ab initio simulations using a TDDFT approach in the linear-response (LR-TDDFT) approximation [111].

In LR-TDDFT simulations, one aims at calculating the polarization function $\chi(\mathbf{r}, t, \mathbf{r}', t')$ relating the perturbation of the density δn at $(\mathbf{r}, t)$ due to a small change of the external potential δv_{ext} at $(\mathbf{r}', t')$:

$$\delta n(\mathbf{r}, t) = \int dt' \int d^3 r' \chi(\mathbf{r}, t, \mathbf{r}', t') \delta v_{\mathrm{ext}}(\mathbf{r}', t') \tag{5.19}$$

The many-body response function $\chi(\mathbf{r}, t, \mathbf{r}', t')$ can be obtained by the independent particle polarizability $\chi_{KS}(\mathbf{r}, t, \mathbf{x}, \tau)$ via a Dyson-type equation as follows:

$$\chi(\mathbf{r},t,\mathbf{r}',t') = \chi_{\mathrm{KS}}(\mathbf{r},t,\mathbf{r}',t')\Big\{\int d\tau \int d^3x \int d\tau' \int d^3x' \\ \chi_{\mathrm{KS}}(\mathbf{r},t,\mathbf{x},\tau)\Big[\frac{\delta(\tau-\tau')}{|\mathbf{x}-\mathbf{x}'|} + f_{\mathrm{xc}}(\mathbf{x},\tau,\mathbf{x}',\tau')\Big] \\ \chi(\mathbf{x}',\tau',\mathbf{r}',t')\Big\} \tag{5.20}$$

where $f_{\mathrm{xc}}(\mathbf{r},t,\mathbf{r}',t') = \frac{\delta v_{\mathrm{xc}}(\mathbf{r},t)}{\delta n(\mathbf{r}',t')}\Big|_{n_{\mathrm{gs}}(\mathbf{r},t)}$ is the energy-dependent exchange-correlation kernel. The independent particle response function χ_{KS} is calculated usually by solving the standard Kohn-Sham equations. As for static DFT, the time-dependent exchange-correlation potential is unknown. Thus, calculations of $\chi(\mathbf{r},t,\mathbf{r}',t')$ usually rely on the so-called adiabatic local-density approximation (ALDA) in which the time dependence of the functional is neglected [110]. However, in systems where excitonic effects are expected to have a strong influence on spectral features due to an ineffective electronic screening, e.g. in insulators such as diamond, the use of a bootstrap kernel [125] that includes effects beyond the RPA is necessary.

Assuming translational invariance, the ELF can be computed inserting Eq. 5.13 into Eq. (5.15). The inversion procedure can be cumbersome for large basis sets and large k-point grids. Thus, wherever possible the most viable option is to assess the microscopic dielectric matrix by inverting only the head of the matrix, which means to neglect the off-diagonal elements ($\epsilon_{\mathbf{G},\mathbf{G}'}(\mathbf{q},W)$, $\mathbf{G},\mathbf{G}' \neq 0$) for all $\mathbf{q}$ [115]. These off-diagonal terms include the fluctuations of the fields on atomic scale, called the local field effects (LFE). Nevertheless, for highly inhomogeneous or strongly locally polarizable systems, such as in the case of diamond and graphite, strong microscopic local fields can exist, and thus LFE can play a significant role in the description of the dielectric properties [126], particularly at small wavelengths, to the point of invalidating even qualitative results. This is the case, for example, of our 3D carbon-based materials, and, thus, we will include LFE in our analysis. With the inclusion of the LFE, one can show that the dielectric function in reciprocal space is [127]:

$$\epsilon^{-1}_{\mathbf{G},\mathbf{G}'}(\mathbf{q},W) = \delta_{\mathbf{G},\mathbf{G}'} + v^{s}_{\mathbf{G},\mathbf{G}'}(\mathbf{q})\chi_{\mathbf{G},\mathbf{G}'}(\mathbf{q},W) \tag{5.21}$$

where $v^{s}_{\mathbf{G},\mathbf{G}'}(\mathbf{q}) = \frac{4\pi e^2}{|\mathbf{q}+\mathbf{G}||\mathbf{q}+\mathbf{G}'|}$ is the Fourier transform of the Coulomb potential and $\chi_{\mathbf{G},\mathbf{G}'}(\mathbf{q},W)$ is the microscopic polarizability.

ELFs and Related Observables of Diamond and Graphite

While for computational details we refer to Ref. [64], using LR-TDDFT we calculated the ELFs of diamond and graphite according to Eq. 5.15. In the top panels of Fig. 5.29, we report the ELFs of diamond (left) and of graphite (right) in comparison to the Drude-Lorentz approach (black lines).

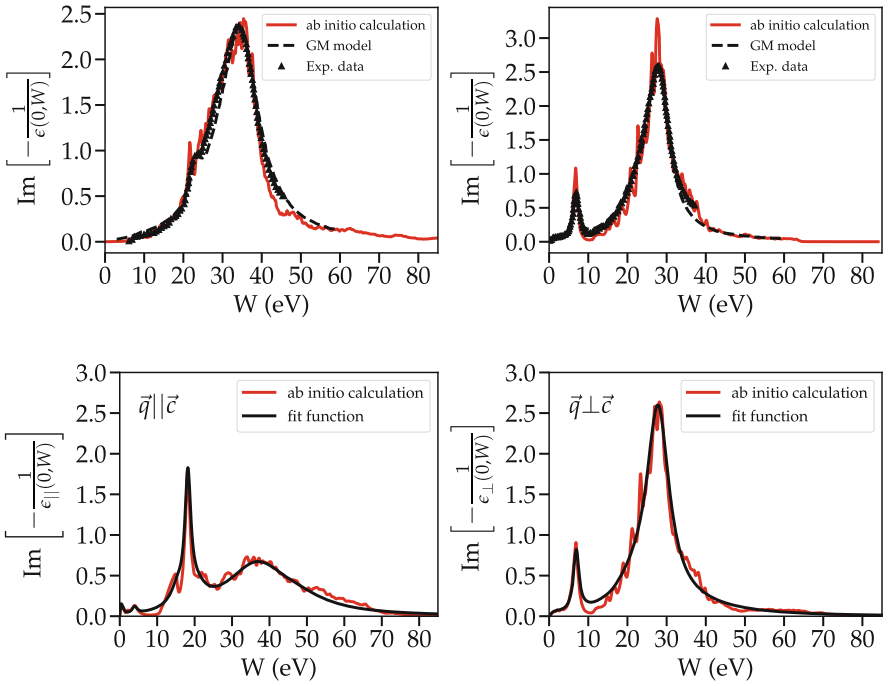

Fig. 5.29 Top panels: Comparison between the ELF of diamond (left) and graphite (right) in the optical limit obtained from AI simulations (continuous red curve), experimental data from Refs. [104] and [105] (black triangles) and fit obtained with the model of Garcia-Molina et al. [123] (dashed black line). Bottom panels: ELF of graphite from AI simulations along the direction $q||c$ (left) and $q \perp c$ (right). (Adapted from Refs. [18] and [64])

Nevertheless, in the case of graphite, one should also take into account the anisotropic structure. This can be achieved by calculating the inverse of the total inelastic mean free path $\Lambda_{inel} = \lambda_{inel}^{-1}$ and the energy loss W as a linear combination along the two directions, respectively, orthogonal ($\perp$) or parallel ($||$) to the vector $\boldsymbol{c}$ pointing towards the direction orthogonal to the graphite plane, as follows [64]:

$$\Lambda_{inel} = f\cos^2(\theta)\Lambda_{||} + [(1-f) + f\sin^2(\theta)]\Lambda_{\perp} \tag{5.22}$$

$$W = f\cos^2(\theta)W_{||} + [(1-f) + f\sin^2(\theta)]W_{\perp} \tag{5.23}$$

where f is an anisotropy parameter in the range $[0:1]$ determined so to obtain the best agreement between theoretical and experimental spectra and θ is the angle between $\boldsymbol{c}$ and $\boldsymbol{q}$. This parameter is put in place to favour the electron motion in the planar direction ($q \perp c$).

In the bottom panels of Fig. 5.29, the contributions to the ELFs of graphite are resolved in the direction parallel $q||c$ (left) and perpendicular $q \perp c$ (right) to the graphite plane obtained from AI simulations (and relevant fits). Finally, in Fig. 5.30 we report the parallel (left panel) and orthogonal (right panel) contributions to the

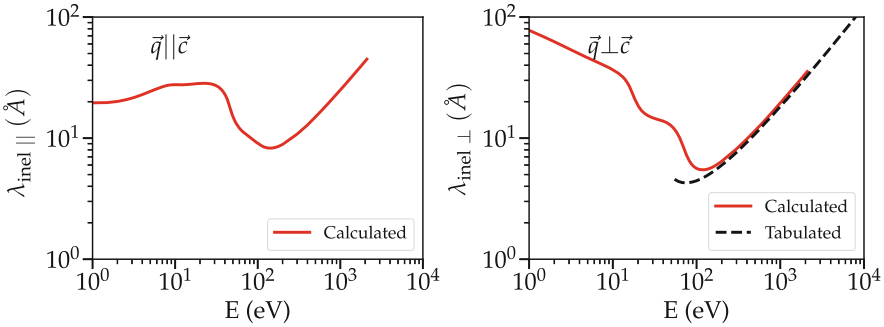

Fig. 5.30 Inelastic mean free path along the parallel (left panel) and orthogonal (right panel) directions of the transferred momentum $\boldsymbol{q}$ in graphite. For $\boldsymbol{q} \perp \boldsymbol{c}$, the calculated values are compared with the data by Tanuma et al. (dashed lines) [124]. (Adapted from Ref. [64])

inelastic mean free path in graphite. These quantities are then used as input to a Monte Carlo approach of the charge transport within solids.

5.6.1.2 Theory of Monte Carlo Simulations

The transport of electrons within a material can be simulated by a classical MC approach, assuming that the non-relativistic electron beam wavelength is small with respect to interatomic separation [118] and that the scattering cross sections for the different processes occurring within materials are known.

At this level the target is assumed to be semi-infinite, homogeneous and amorphous, the latter conditions supporting the assumption of incoherent scattering between different events. In our transport model, we consider a monoenergetic N-electron beam impacting on the target with kinetic energy T and angle of incidence θ with respect to the surface normal.

Electrons can undergo elastic and inelastic scattering. The scattering is usually elastic when electrons scatter nuclei with far heavier mass, and only a trajectory change by an angle θ is recorded. In this case, the elastic cross section σ_{el} is calculated by using the Mott theory, which is based on the solution of the Dirac equation in a central field [117]. In contrast, inelastic scattering processes resulting in both an energy loss W and a directional change θ are mainly due to electron-electron interactions.

Our MC algorithm proceeds by assuming that the path travelled by a test charge between two subsequent collisions is Poisson-distributed, so that the cumulative probability that the electron goes a distance Δs before colliding is given by:

$$\Delta s = -\lambda \cdot \ln(r_1) \tag{5.24}$$

The random numbers r_1, as well as all random numbers employed in our MC simulations, are sampled in the range [0,1] with a uniform distribution. A second

random number r_2 is compared with the elastic ($p_{\text{el}} = \frac{\lambda_{\text{el}}}{\lambda\text{el}+\lambda\text{inel}}$) and inelastic ($p_{\text{inel}} = 1 - p_{\text{el}}$) scattering probabilities to determine whether the scattering is elastic ($r_2 < p_{\text{el}}$) or inelastic ($r_2 \geq p_{\text{el}}$). The algorithm to determine which move is accepted or refused resembles the Bortz-Kalos-Lebowitz kinetic Monte Carlo approach [128] rather than the typical Metropolis algorithm.

The outcome of an elastic interaction is given by the trajectory deflection of an angle θ' with respect to the direction before the collision, which can be computed by equalizing the following cumulative elastic probability with a third random number r_3:

$$P_{\text{el}}(\theta', T) = \frac{1}{\sigma_{\text{el}}} 2\pi \int_0^{\theta'} \frac{d\sigma_{\text{el}}}{d\theta} d\theta = r_3 \tag{5.25}$$

On the other hand, inelastic processes are dealt with by computing the inelastic scattering probability as:

$$P_{\text{inel}}(W, T) = \frac{1}{\sigma_{\text{inel}}} \int_0^{W} \frac{d\sigma_{\text{inel}}}{dW'} dW' = r_4 \tag{5.26}$$

As customary in electronic transport MC calculations, the maximum energy loss corresponds to half of the kinetic energy of the incident electron, to comply with the indistinguishability principle of identical particles. To determine the energy loss W, we generate a database of P_{inel} values for different W and T, and we equalize the integral in Eq. 5.26 to a random number r_4.

Eventually, scattered electrons can be ejected from the target. This ejection can be assessed by a quantity that is called the secondary emission yield (δ). The latter is given by the ratio between the number of secondary electrons emitted from the target material and the number of electrons of the primary beam. The assessment of the secondary electron spectral features is particularly important in imaging techniques [129, 130]. In their way out of the solid, the electrons lose further energy to overcome the potential barrier E_{A} (electron affinity or work function) at the surface of the material. This process can be modelled as scattering by a potential barrier. Thus, the transmission coefficient can be computed as follows:

$$t = \frac{4\sqrt{(1 - E_{\text{A}}/(T \cdot \cos^2\theta'_z))}}{(1 + \sqrt{(1 - E_{\text{A}}/(T \cdot \cos^2\theta'_z))})^2} \tag{5.27}$$

where t represents the probability that the electron leaves the sample's surface and θ'_z is the incident angle with respect to the surface normal. Finally, by comparing this transmission coefficient with a random number r_5, electrons are (or are not) emitted into the continuum with a kinetic energy lowered by the work function E_{A} whenever $t \geq r_5$ ($t < r_5$). By definition, emitted electrons emerging with kinetic energies below 50 eV are called secondary electrons. The Monte Carlo routines used

for performing these simulations are embedded in the in-house developed code suite *SURPRISES* [131–133].

5.6.1.3 Monte Carlo Simulations of Energy-Loss Spectra and Secondary Electron Yield

Diamond

To compare our experimental REELS data of diamond with the three different models of ELF presented above, we performed Monte Carlo (MC) simulations following the scheme reported in Sect. 5.6.1.2. In our MC simulations, diamond crystals are approximated by a homogeneous system with density 3.515 g/cm^3 [123]. Thus, in our simulations we assume that the ELF is almost similar in all directions, and thus we can retain our simulated ELF along the ΓL direction only for calculating the energy-loss spectra. The band gap of diamond was set equal to 4.16 eV. The electron beam direction is orthogonal to the target surface, and the initial kinetic energy ranges from 250 to 2000 eV. The number of impinging electrons is 10^9.

First, we notice that in our treatment we define more generally as backscattered electrons those beam electrons that are reflected back out of the specimen after both elastic and inelastic collisions. In Fig. 5.31 spectra of backscattered electrons simulated in terms of the three different models of the ELF are compared with our REELS experimental data. Simulated and experimental spectra present the σ plasmon peak at ∼35 eV, related to the four valence electrons of the equivalent covalently bonded carbon atoms. This finding is in agreement with the ELF function in the top left panel of Fig. 5.29, showing a maximum at about the same energy.

Furthermore, the two-plasmon excitation at higher energy (∼70 eV) in the experimental spectrum is also present in our MC simulations. We observe that while the MC simulations carried out using the dispersion law of Eq. 5.17 show a blue shift with respect to experimental data, the use of a full AI approach results in a better

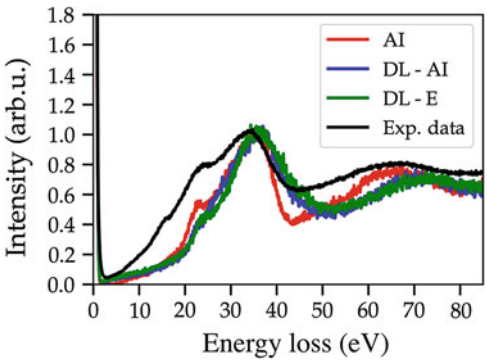

Fig. 5.31 REELS of diamond: experimental data are reported in black, while simulated results using the three different dielectric models are sketched in red (AI), blue (DL-AI) and green (DL-E). Electron beam kinetic energy is 1000 eV. Data are normalized with respect to the σ plasmon peak. (Adapted from Ref. [18])

agreement with experiments. We can conclude that at least in the case of insulators, due to the strongly inhomogeneous electron density and, thus, to the complexity of the dielectric response, the DL model is quantitatively less accurate than a full AI approach in the prediction of the experimental REELS. This behaviour worsens at higher transferred momenta, where particle-hole excitations, rather than collective plasma excitation, come into play. Single-particle excitations generally cannot be well described by a simple RPA or by the DL model of the ELF, while TDDFT AI simulations are also able to take into account these spectral features.

Graphite

Highly oriented pyrolytic graphite (HOPG) crystals were considered to have a density of 2.25 g/cm^3 [123]. The band gap was set equal to 0.06 eV according to our DFT calculations. MC simulations of REELS were carried out using the three different approaches to the calculation of the ELF mentioned above, with a number of electrons in the beam equal to 10^9. Initially, only the in-plane component of the energy-loss function was dealt within the calculation (i.e. we considered the component of the momentum transfer only along the graphite layers). In Fig. 5.32 we report the MC REELS simulations compared to our experimental measurements (black line).

We notice that our MC simulations reproduce both the π (due to the collective excitation of valence electrons in the π band) and the $\pi + \sigma$ (due to collective excitation of all valence electrons) plasmon peaks. These findings are in agreement with the ELF function in the top right panel of Fig. 5.29, showing maxima at about the same energies. While the results of the simulations show good agreement with experimental data independently of the ELF model, nevertheless, using the ab initio calculated ELF at finite momentum transfer, a third peak around 60 eV can be found. This peak corresponds to two-plasmon excitation, and its presence is less

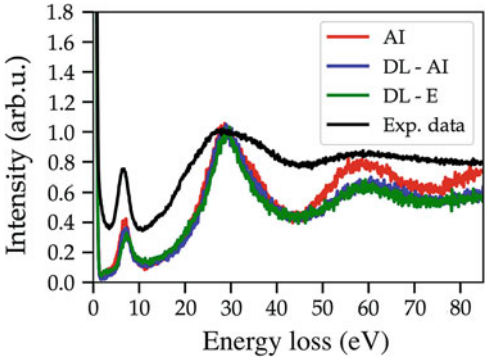

Fig. 5.32 REEL of graphite: experimental data are reported in black, while simulations using the three different models are sketched in red (AI), blue (DL-AI) and green (DL-E). Electron beam kinetic energy is 1000 eV. Data are normalized with respect to the $\pi + \sigma$ plasmon peak. (Adapted from Ref. [18])

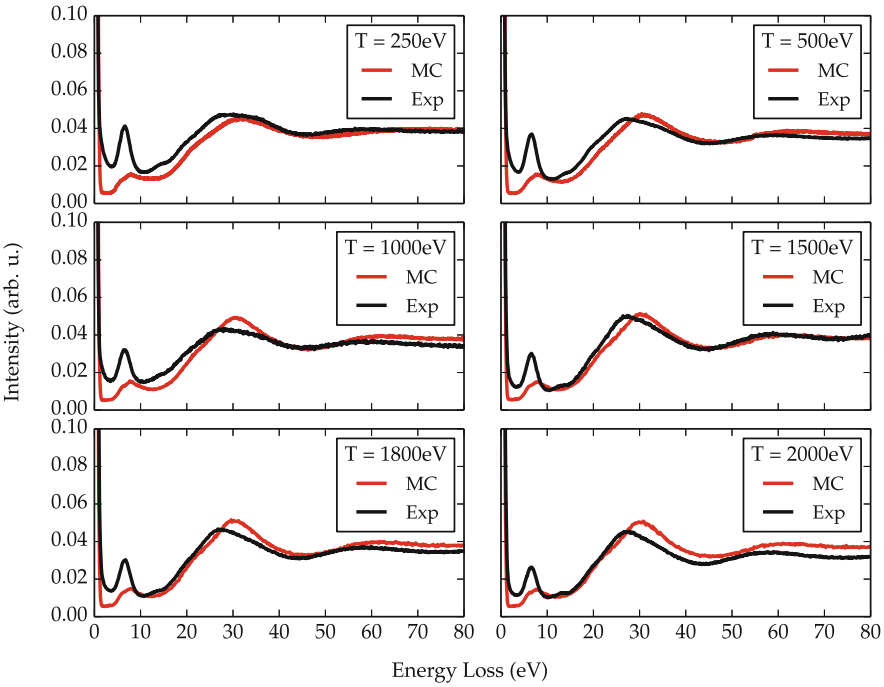

Fig. 5.33 REELs of HOPG for several primary beam kinetic energies. Red lines show simulated spectra, while black curves report our experimental data [18]. The results are normalized at a common area of the elastic peak. (Adapted from Ref. [64])

apparent by adopting DL models. Indeed, in DL models the RPA approximation describes the system as composed of free electrons; in the case of graphite, the electrons populating the π bands are delocalized, and they behave as almost-free electrons. For this reason, the π plasmon peak is prominent in all three spectra. The discrepancies found in the energy-loss spectral features recommend the use of AI approaches for the extension of the ELF out of the optical region, in order to deal accurately with the electronic motion inside the material.

Furthermore, we performed REEL spectra MC simulations at several primary beam kinetic energies for a value of the anisotropy parameter $f = 0.6$, which provides the best agreement between experimental and calculated REELS (see Fig. 5.33). This anisotropic model is consistent with the higher tendency of the electrons to move along the graphite planes rather than across the planes.

Finally, the assessment of secondary electron (SE) spectra and yield is crucial in imaging techniques. SE emission from graphite was thus assessed by MC simulations, using a kinetic energy of the incident beam ($N = 10^6$) equal to 1000 eV. In Fig. 5.34 we compare our MC calculations with the acquired experimental spectra.

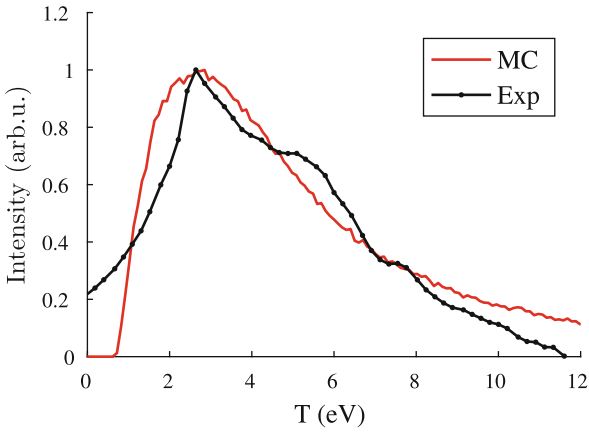

Fig. 5.34 Secondary electron spectra of HOPG. Black line represents experimental data, while in red we report the theoretical spectrum. The data are normalized to a common height of the secondary electron emission peak. (Adapted from Ref. [64])

5.6.2 Graphite for Armour Technologies

The study of ballistic properties of layered two-dimensional materials upon the hypervelocity impacts is an important topic for the protection of structures and devices from the penetration of highly energetic projectiles [61]. In particular, in this section we describe the impact of C_{60} molecules on graphite.

While the critical penetration energy of monolayer membranes can be determined using monolayers, the synergistic behaviour of multilayered structures, such as graphite, depends dramatically on the interface characteristics (e.g. adhesive strength). Indeed, in some occasions, the layer coupling may not be effective. This effect can be expressed using the following energy absorption scaling law:

$$\frac{K_{abs}(N)}{N} = K \times N^{\alpha} \tag{5.28}$$

where K is a constant. A scaling exponent $\alpha > 0$ indicates a synergistic behaviour in which single layers interact to mutually enhance their specific contribution. On the other hand, for $\alpha = 0$, the total absorbed energy is the mere sum of single-layer contributions, whereas for $\alpha < 0$ a suboptimal behaviour is identified in which increasing the number of layers leads to worse or inefficient interlayer coupling.

At the nanolevel, we find by impinging C_{60} fullerene on graphite samples that a synergistic interaction between the graphene layers emerges, whereby an optimal number of layers, between 5 and 10, can be identified demonstrating that few-layered 2D material armours possess impact strength even higher than their monolayer counterparts. In Fig. 5.35 we report the representation of the optimal number of layers, which corresponds to both the maximum specific energy absorption by strain and the inversion in the sign of the scaling exponent of Eq. 5.28.

These results provide fundamental understanding for the design of ultralight weight multilayer armours using enhanced 2D material-based nanocomposites.

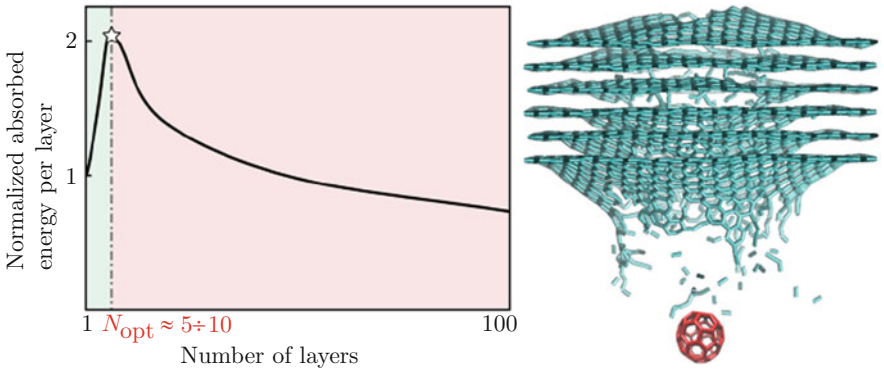

Fig. 5.35 Representation of the optimal number of layers, which corresponds to both the maximum specific energy absorption by strain and the inversion in the sign of the scaling exponent of Eq. 5.28. (Adapted from Ref. [61])

5.6.3 Other 3D Carbon Materials: Foams and Graphene Frameworks

5.6.3.1 Graphene Foams

Graphene foams are all-carbon 3D structures made by big fullerenes connected through carbon nanotubes (see top panels of Fig. 5.36), so they possibly represent relics of the mechanical and thermal properties of graphene. Recently, they have attracted interest for their possible use as electrochemical storage devices, in wearable electronics, in chemical sensing and as impact energy absorbers [63, 65].

In particular, one can assess the mechanical and thermal performances of foams characterized by increasing mass density and decreasing average pore size. In the bottom panels of Fig. 5.36, we show the mechanical performances under compression for regular (bottom left) and random (bottom right) foams. Regular foams are nanotruss networks characterized by some degree of crystallinity with face-centred cubic geometry (these are shown in the top left panel of Fig. 5.36). It is worthwhile noticing that the mechanical response of regular foams to loading depends on the ratio between the nanotube and the sphere diameters (see bottom left panel of Fig. 5.36). In the case of random foams, where pore positions and dimensions are random (see top right panel of Fig. 5.36), the higher-density foams show the typical slope change in the stress-strain curve at 5–10% strain, moving from linear elasticity to bending stress plateau, and lower density foams display a quasilinear behaviour up to 35% strain (see bottom right panel of Fig. 5.36). We conclude that in both crystalline and random foams, we observe the typical elastic deformation regime under compression, with a specific Young's modulus significantly increasing with a decreasing average pore size. Nevertheless, some of these nanotruss networks present a negative Poisson's ratio in compression, like re-entrant foams. Furthermore, for nanotruss network, at 5–8% strain, the stress is

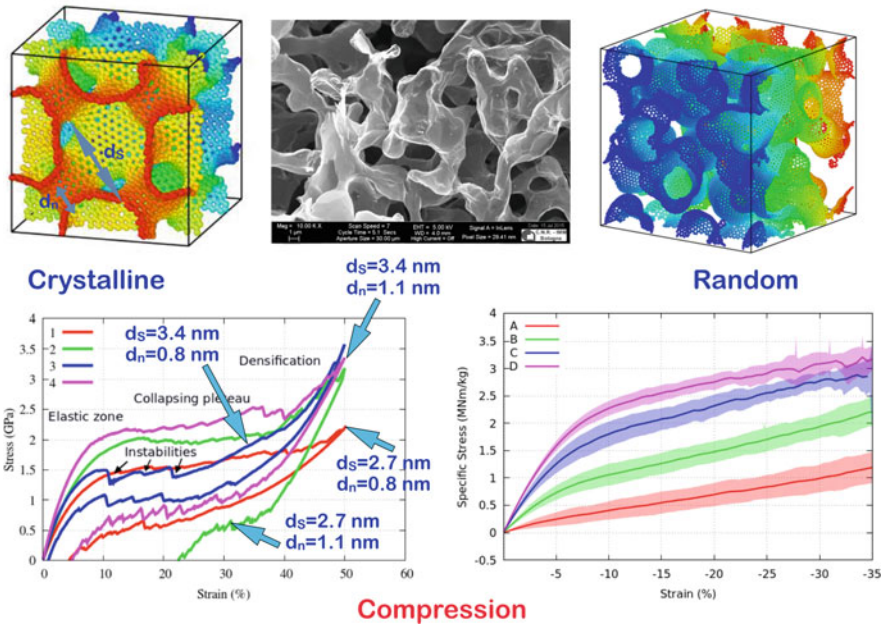

Fig. 5.36 Top panels: crystalline and random graphene-like foams. Bottom panels: stress-strain curves of crystalline (left) and random (right) foams with different sphere (d_s) and tube (d_n) diameters in compressive regime. Middle: electron microscopy image of a graphene random foam (courtesy of CNR-IMM Bologna, Italy). (Adapted from Refs. [63, 65])

in the range 90–130 MNm kg^{-1}, while for random foams at the same strain, the values are in the range 3.9–36.6 MNm kg^{-1}. This makes clear that regular foams are mechanically stiffer than the random ones.

Finally, owing to the interest of using foams as a mean for achieving thermal resistance, we assess the thermal conductivity of the random foams using the equilibrium Green-Kubo approach [134, 135]. According to this formalism, the equilibrium thermal conductivity k can be calculated as follows:

$$k = \frac{V}{3K_B T^2} \int_0^\infty \langle \boldsymbol{J}(0) \cdot \boldsymbol{J}(t) \rangle dt \tag{5.29}$$

where V is the volume of the simulation cell, t is the correlation time, K_B is the Boltzmann constant and $\boldsymbol{r}$ identifies the particle positions. The heat current $\boldsymbol{J}$, appearing in Eq. 5.29, is defined by:

$$\boldsymbol{J} = \frac{1}{V}\Big(\sum_i E_i \boldsymbol{v}_i + \frac{1}{2} \sum_{i<j} (\boldsymbol{F}_{ij} \cdot (\boldsymbol{v}_i + \boldsymbol{v}_j) \boldsymbol{r}_{ij}) \Big) \tag{5.30}$$

where $\boldsymbol{v}$ is the velocity of a particle, $\boldsymbol{r}_{ij}$ and $\boldsymbol{F}_{ij}$ are the distance and force between the particles i and j and E_i is the total energy per atom. The first term in the

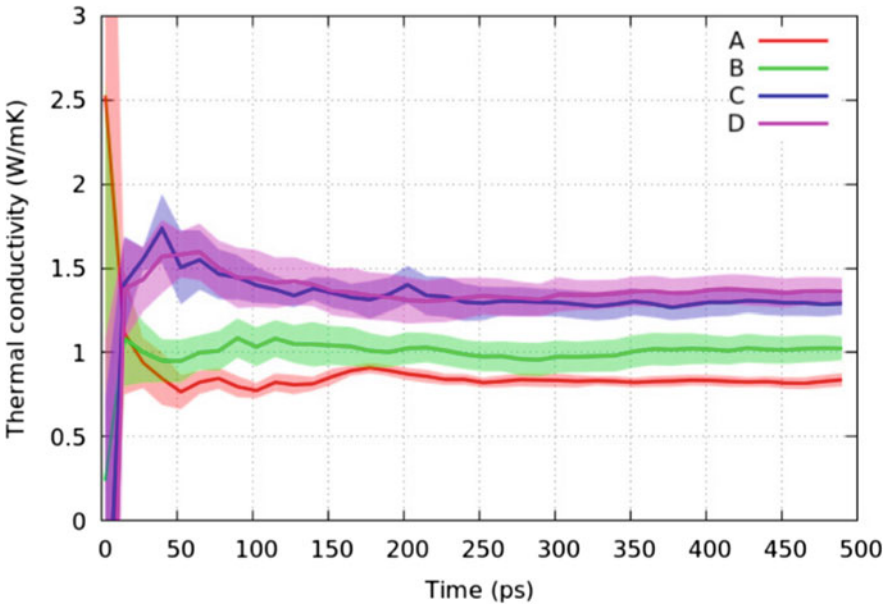

Fig. 5.37 Time averaged vs. simulation time of the four random foam families calculated as by Eq. 5.29. The asymptotic values after 300 ps provide the thermal conductivity of the samples. The shaded area for each relevant curve represents half of the standard deviation. (Adapted from Ref. [63])

right-hand side of Eq. 5.30 corresponds to convection while the second term to conduction. The integrand in the expression 5.29 of the thermal conductivity is the heat current autocorrelation function (HCACF). While foam thermal conductivity is affected by both connectivity and defects, nevertheless we obtain similar values for all the investigated families. The thermal conductivity, reported in Fig. 5.37, is comparable to that of glass, thus higher than materials typically used as thermal insulators, such as polyurethane rigid foams.

5.6.3.2 Pillared Graphene

Pillared Graphene Frameworks (PGF) are a novel class of microporous materials made by graphene sheets separated by organic spacers [136, 137]. One of their main features is that the pillar type and density can be chosen to tune the capacity of the material to, e.g. adsorb gases or separate gas mixtures. Pillars are typically made by organic rigid molecules, containing carbon and/or nitrogen (see top panels of Fig. 5.38). In general, the pillar density plays the most important role in determining gas adsorption rather than the chemical typology of the spacers. In the low-pressure regime ($\lesssim$10 bar), the amount of gas adsorbed is an increasing function of pillar density. At higher pressures the opposite trend is observed. This effect is

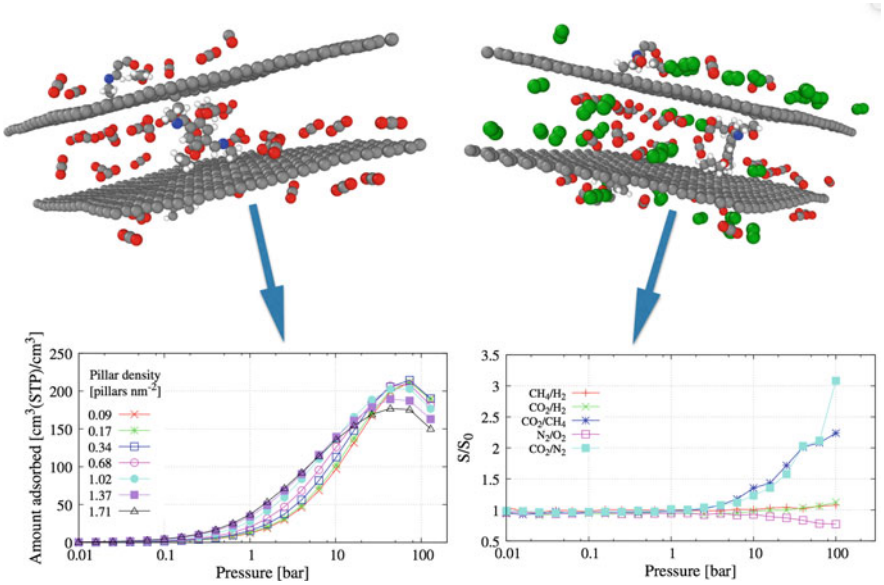

Fig. 5.38 Top: typical PGFs with nitrogen and organic based pillars. Bottom left: Volumetric adsorption isotherms of CH_4 at $T = 298$ K in PGF. Bottom right: Selectivity for gas mixtures at $T = 298$ K, normalized with respect to the zero-pressure limit value of selectivity (S_0). (Reproduced by adapting figures from Ref. [136])

clearly visible in the bottom left panel of Fig. 5.38, where the volumetric uptake of CH_4 vs. pressure is plotted. Other than adsorption, PGF can be used to sieve gas binary mixture, such as CH_4/H_2, CO_2/H_2 and CO_2/N_2. The dynamic of the mixture passing through the pillared structures can be simulated by assessing the diffusion coefficients taking into account the framework flexibility that is essential in assessing the dynamical properties of the adsorbed gases. Good performance for the gas separation in mixtures was found with values comparable to those of metal-organic frameworks (MOFs) and zeolites (ZIFs) [138, 139]; see bottom right panel of Fig. 5.38.

5.7 Conclusions and Future Outlook

The first goal of this chapter was to demonstrate the impact that dimensionality has in the emergence of novel properties at nanoscale. Climbing up the "ladder of dimensionality", from 0D to 3D, we discussed a variety of systems using several all-carbon-based materials as role models of our analysis.

In particular, we used fullerene, the spherically shaped 0D carbon allotrope, accelerated to supersonic velocities to demonstrate the factual possibility to synthe-

size graphene sheets at low temperature via our in-house SuMBE growth technique. While we did not succeed for technological limitations to lower the working temperature down to room conditions at variance with the case of SiC growth, however SuMBE was capable of synthesizing a fairly even coating of graphene-like material in a single layer at 645 °C using H_2 as carrier gas. This temperature is remarkably smaller than that of other widely used approaches, such as CVD (in excess of 900 °C), MBE of C_{60} on Ru(0001) (725 K for the cage thermal break and 1200 K for complete monolayer formation) [140] or on noble metals (1050 K) [141]. Graphene nano-islands, even according to our metadynamics simulations, are not made of regular hexagons, like in pristine graphene, but also contain pentagons, which come from the original buckyball structures. We notice that this characteristic is potentially useful, because the pentagonal defects introduce a band gap into the material, something materials scientists have longed hoped to create in graphene. Although at this stage we believe that our results represent a proof of principle, the technique looks interesting, not least because it produces relatively high-quality films and could also be applied using a wide range of materials as a substrate, such as semiconductors and insulators avoiding the graphene layer transfer from the growth substrate to different substrates for producing high-end electronic devices.

We then discussed a systematic approach for generating bi-dimensional all-sp^2 carbon allotropes, aiming at decreasing the density of graphene without depleting its unique mechanical properties. This method proceeds by augmenting the number of congruent discs under the constraint of local stability. The daughter structures share the common drawbacks of having lower stability and smaller cohesive energy than graphene, while their density is reduced by 45% with respect to graphene. In particular, we conclude that (i) flakene may represent the least dense possible architecture among the families of bi-dimensional all-sp^2 carbon allotropic forms under the local stability constraints; (ii) the augmentation increases the metallicity character of the daughter structures with respect to parent ones; (iii) while the absolute stress-strain characteristics are definitely depleted by augmentation, also a threshold exists below which one cannot reduce further the density without a considerable performance loss of the specific mechanical properties; (iv) tilene parent displays a specific strength higher than graphene; and (v) finally, graphene presents one of the highest specific modulus ever found, and the quest for finding a better replacement in mechanical engineering applications is still open.

Graphene can be also rolled in the shape of nanotubes, and we have showed, using a GW approach based on the expansion of the polarizability operator in an optimal basis, how the electronic band gap of semiconducting CNTs evolves by increasing the tube size. This approach allows one to avoid the explicit sum over the unoccupied states while allowing for good accuracy. We showed that an accurate estimate of the excitation binding energies can be achieved by coupling optical measurements with theoretical modelling [93, 95]. We extrapolated the gap vs. diameter function for large dimensions showing that this dependence can be modelled by $E_{\text{gap}} = 1.54\ \text{eV} \times \text{nm}$. This relation is found to be in good agreement with a recent direct measurement of the electronic gap performed via STS for the case of 1.4 nm diameter CNT [91].

In the 3D case of study, we assessed the frequency-dependent dielectric response and energy-loss functions of diamond and graphite in two ways: a full ab initio approach, in which we carry out time-dependent density functional simulations in linear response for different momentum transfers, and a semiclassical model, based on the Drude-Lorentz extension to finite momenta of the optical dielectric function. We conclude that ab initio calculated dielectric functions lead to better agreement with measured energy-loss spectra compared to the widely used Drude-Lorentz model. This discrepancy is particularly evident for insulators and semiconductors beyond the optical limit ($\mathbf{q} \neq 0$), where single-particle excitations become relevant. Furthermore, we show that the behaviour of the energy-loss function obtained at different accuracy levels has a dramatic effect on other physical observables, such as the inelastic mean free path and the stopping power in the low energy ($<100\,\mathrm{eV}$) regime and thus on the accuracy of MC simulations of REEL spectra. Thus, the major point of this work is to show that an accurate treatment of the electron-electron correlations beyond the random-phase approximation of the homogeneous Fermi gas is necessary to increase the overall accuracy of the simulations to be compared with REEL experiments. We also discuss a theoretical approach for taking into account the anisotropic structure of HOPG in the Monte Carlo simulations of charge transport. The anisotropic description of the dielectric response is achieved by linearly combining the contributions to the inverse inelastic mean free path and energy losses along the two main orthogonal directions identifying the layered crystalline structure of graphite. Monte Carlo simulated spectra, obtained with our anisotropic approach, are compared with acquired experimental data of reflection electron energy loss and secondary electron spectra, showing a good agreement. These findings validate the idea of the importance of considering properly weighted interplanar and intra-planar interactions in the simulation of electron transport in layered materials.

Furthermore, we discussed the mechanical behaviour of single and multilayer graphene armours subjected to hypervelocity impacts of fullerene molecules, due to their outstanding mechanical stability. The investigation of the interlayer synergy between adjacent layers at the nanoscale determines that an optimal number of layers, between 5 and 10, emerges that maximizes also the specific energy dissipation under impact. These results suggest that multilayer 2D material-based armours should be structured and optimized at the nanolevel, not relying on the mere high-specific mechanical properties of the constituent materials.

Finally, we studied the mechanical properties of nanotruss networks and of random foams, as a further example of 3D materials based on carbon. In this respect, we conclude that nanotruss networks and random foams may represent exceptional candidates for porous, flexible and high-strength materials. Basically they inherit the marvellous mechanical properties of the parent material, graphene, adding a third bearing stress dimension. In applications to gas adsorption and sieving, other convenient 3D architectures are represented by the PGFs. Our results show that the density of pillars dramatically affects the adsorption rather than the pillar type as, under saturation conditions, the increase of pillar density results in a sensible decrease of the amount of gas adsorbed.

After having discussed the marvellous properties that carbon nanomaterials acquire by moving up the dimensionality ladder, we believe meaningful to provide an outlook about the foreseeable impact that over the next decades carbon-based materials can have in defining the reach and applications of nanotechnology. Indeed, the versatility of carbon to make bonds with itself and also other chemical elements with different hybridization levels represents the most striking feature which allows to use it in different technological scenarios. In the last three decades, starting from the discovery of fullerenes, carbon nanotube (CNT), graphene and other 2D materials, we have been flush with novel ideas and innumerable attempts to find the killer applications for these remarkable nanostructures. For example, nearly two decades of research in graphene fundamental properties have landed potential influence on longer-lasting batteries, more efficient solar cells, transparent and wearable faster electronics, novel LCD and OLED display panels, data storage devices as well as novel approaches to electrochemical sensing in medicinal technologies or to reinforcing composite matrices to enhance their mechanical properties. Significant breakthrough in our everyday life can also come from the revival of CNT-based technologies, such as in the production of transparent electrodes due to their high conductivity, which allows the construction of ultra-thin films (1–100 nm). Additionally, one can exploit CNTs for solving environmental issues due to their promising catalytic properties, such as in pollution remediation, and energy-related problems, such as in the search for alternative energy sources to replace the use of fossil fuels or the production of H_2 via water splitting due to the large number of active adsorption sites.

Nevertheless, we notice that so far, despite the many worldwide efforts to advance carbon-based technology by using CNT or graphene, very few real-world applications benefit from the potential that these materials display. This still missing carbon revolution to replace silicon as the material of the future electronics seems to be due to factors such as mass production and sample quality. For example, the requirement of large-area, defect-free, grain boundary-free, monocrystalline graphene to date has not been yet achieved. Furthermore, the question of whether CNTs and graphene are the right choices for mechanical reinforcement still remains largely unanswered, basically due to adhesion issues at the interface. Nevertheless, with the great deal of interest in carbon-based technologies, it would not be surprising if the first commercially available applications could be already found in the next decade timeframe. Still, we believe that what makes CNTs and graphene so special is beyond their technological applications, as they represent a paradigm of a new class of mono- and bi-dimensional materials, whose discovery and study clearly date from its synthesis. Furthermore, the electrical conductivity, the electronic structure and the optical properties of carbon-based materials can be easily tuned by heteroatom doping in order to adjust their electron mobility, charge transfer capacity and optical response. For example, due to the potential applications as a basic unit of a quantum computer, in quantum cryptography, spintronics and masers, recently nitrogen-vacancy centre (N-V centre) in diamond gained a lot of attention in the scientific community. Indeed, its most investigated and potentially useful property is photoluminescence, which can be easily detected from an individual N-V centre.

Electron spins localized at N-V centres can be manipulated at room temperature by applying magnetic or electric fields, resulting in sharp resonances in the intensity and wavelength of the photoluminescence. These resonances can be rationalized in terms of quantum entanglement, spin-orbit interaction and Rabi oscillations and analysed using advanced quantum optics theory.

As a final remark, we strongly believe that there is a great need for research and development of new technologies involving the reduction of environmental impacts, seeking the use of renewable raw and low-cost materials. In this regard, carbon-based nanomaterials, such as ultra-thin carbon films, can play a major role [142].

Acknowledgements S.T. acknowledges invaluable discussions with several colleagues who helped him to develop the methods described in this chapter and to carry out the computational modelling presented. In particular, we mention Dr. M. Azzolini, Dr. M. Dapor, Dr. G. Garberoglio, Dr. T. Morresi, Dr. A. Pedrielli, prof. N. Pugno and Dr. S. Simonucci. This chapter is basically the outcome of a decade-long collaboration with all of them.

References

1. P.W. Anderson, More is different. Science **177**, 393–396 (1972)
2. G. Gallavotti, *Statistical Mechanics*. Texts and Monographs in Physics. (Springer, Berlin, 1999)
3. C.G. Smith, Low-dimensional quantum devices. Rep. Prog. Phys. **59**, 235–282 (1996)
4. A.H. Castro Neto, F. Guinea, N.M.R. Peres, K.S. Novoselov, A.K. Geim, The electronic properties of graphene. Rev. Mod. Phys. **81**, 109–162 (2009)
5. K.S. Novoselov, A. Mishchenko, A. Carvalho, A.H. Castro Neto, 2D materials and van der Waals heterostructures. Science **353**, 461–472 (2016)
6. P.J. Burke, Nanotubes and nanowires. (World Scientific, Singapore, 2007)
7. T. Morresi, M. Timpel, A. Pedrielli, G. Garberoglio, R. Tatti, R. Verucchi, L. Pasquali, N. Pugno, M.V. Nardi, S. Taioli, A novel combined experimental and multiscale theoretical approach to unravel the structure of SiC/SiO_x core/shell nanowires for their optimal design. Nanoscale **10**, 13449–13461 (2018)
8. S. Iijima, Helical microtubules of graphitic carbon. Nature **354**, 56–58 (1991)
9. X. Wang, Q. Li, J. Xie, Z. Jin, J. Wang, Y. Li, K. Jiang, S. Fan, Fabrication of ultralong and electrically uniform single-walled carbon nanotubes on clean substrates. Nano Lett. **9**, 3137–3141 (2009)
10. C.D. Spataru, S. Ismail-Beigi, L.X. Benedict, S.G. Louie, Excitonic effects and optical spectra of single-walled carbon nanotubes. Phys. Rev. Lett. **92**, 077402 (2004)
11. P. Umari, O. Petrenko, S. Taioli, M.M. De Souza, Communication: electronic band gaps of semiconducting zig-zag carbon nanotubes from many-body perturbation theory calculations. J. Chem. Phys. **136**, 181101 (2012)
12. S. Taioli, P. Umari, M.M. De Souza, Electronic properties of extended graphene nanomaterials from *GW* calculations. Phys. Status Solidi (B) **246**, 2572–2576 (2009)
13. R.C. Ashoori, Electrons in artificial atoms. Nature **379**, 413–419 (1996)
14. W.G. Van der Wiel, S. De Franceschi, J.M. Elzerman, T. Fujisawa, S. Tarucha, L.P. Kouwenhoven, Electron transport through double quantum dots. Rev. Mod. Phys. **75**, 1–22 (2002)
15. A. Imamoglu, Are quantum dots useful for quantum computation? Phys. E Low Dimens. Syst. Nanostruct. **16**, 47–50 (2003)

16. L. Van Hove, The occurrence of singularities in the elastic frequency distribution of a crystal. Phys. Rev. **89**, 1189–1193 (1953)
17. F. Bassani, G. Pastori Parravicini, *Electronic States and Optical Transitions in Solids* (Pergamon Press, Oxford/New York, 1975)
18. M. Azzolini, T. Morresi, G. Garberoglio, L. Calliari, N.M. Pugno, S. Taioli, M. Dapor, Monte Carlo simulations of measured electron energy-loss spectra of diamond and graphite: role of dielectric-response models. Carbon **118**, 299–309 (2017)
19. P. Cudazzo, M. Gatti, A. Rubio, Interplay between structure and electronic properties of layered transition-metal dichalcogenides: comparing the loss function of $1T$ and $2H$ polymorphs. Phys. Rev. B **86**, 075121 (2012)
20. C.L. Kane, E.J. Mele, Quantum spin hall effect in graphene. Phys. Rev. Lett. **95**, 22680 (2005)
21. H. Gao, Application of fracture mechanics concepts to hierarchical biomechanics of bone and bone-like materials. Int. J. Fract. **138**, 101–137 (2006)
22. H. Yao, H. Gao, Multi-scale cohesive laws in hierarchical materials. Int. J. Solids Struct. **44**, 8177–8193 (2007)
23. M.J. Buehler, S. Keten, T. Ackbarow, Theoretical and computational hierarchical nanomechanics of protein materials: deformation and fracture. Prog. Mater. Sci. **53**, 1101–1241 (2008)
24. R. Puxkandl, I. Zizak, O. Paris, J. Keckes, W. Tesch, S. Bernstorff, P. Purslow, P. Fratzl, Viscoelastic properties of collagen: synchrotron radiation investigations and structural model. Philos. Trans. R. Soc. Lond. B **357**, 191–197 (2001)
25. M.S. Dresselhaus, G. Dresselhaus, P.C. Eklund, Science of fullerenes and carbon nanotubes (Academic Press, San Diego, 1996)
26. D.E.H. Jones, Hollow molecules. New Sci. **32**, 245 (1966)
27. H.W. Kroto, J.R. Health, S.C. O'Brien, R.F. Curl, R.E. Smalley, C60: Buckminsterfullerene. Nature **318**, 162–163 (1985)
28. A. Lassesson, N. Walsh, F. Martinez, A. Herlert, G. Marx, L. Schweikhard, Formation of fullerene dianions in a Penning trap. Eur. Phys. J. D At. Mol. Opt. Plasma Phys. **34**, 73–77 (2005)
29. D. Tomànek, M.A. Schluter, Growth regimes of carbon clusters. Phys. Rev. Lett. **67**, 2331–2334 (1991)
30. C.J. Brabec, E.B. Anderson, B.N. Davidson, S.A. Kajihara, Q.-M. Zhang, J. Bernholc, D. Tomànek, Precursors to C_{60} fullerene formation. Phys. Rev. B **46**, 7326–7328 (1992)
31. Z. Yufeng, K. Yong-Hyun, A.C. Dillon, M.J. Heben, S.B. Zhang, Hydrogen storage in novel organometallic buckyballs. Phys. Rev. Lett. **94**, 155504 (2005)
32. C.E. Housecroft, A.G. Sharpe, Chapter 14: the group 14 elements, in *Inorganic Chemistry*, 3rd edn. (Pearson, London, 2008)
33. N.S. Sariciftci et al., Semiconducting polymer-buckminsterfullerene heterojunctions: diodes, photodiodes, and photovoltaic cells. Appl. Phys. Lett. **62**, 585–587 (1993)
34. F. Tran, P. Blaha, Accurate band gaps of semiconductors and insulators with a semilocal exchange-correlation potential. Phys. Rev. Lett. **102**, 226401 (2009)
35. S. Jalali-Asadabadi, Electronic structure of crystalline buckyballs: fcc-C_{60}. J. Electron. Mater. **45**, 339–348 (2016)
36. E.L. Shirley, S.G. Louie, Electron excitations in solid C_{60}: energy gap, band dispersions, and effects of orientational disorder. Phys. Rev. Lett. **71**, 133–136 (1993)
37. K.H. Michel, J.R.D. Copley, D.A. Neumann, Microscopic theory of orientational disorder and the orientational phase transition in solid C_{60}. Phys. Rev. Lett. **68**, 2929–2932 (1992)
38. S. Saito, A. Oshiyama, Cohesive mechanism and energy bands of solid C_{60}. Phys. Rev. Lett. **66**, 2637–2640 (1991)
39. M.S. Golden, M. Knupfer, J. Fink, J.F. Armbruster, T.R. Cummins, H.A. Romberg, M. Roth, M. Sing, M. Schmidt, E. Sohmen, The electronic structure of fullerenes and fullerene compounds from high-energy spectroscopy. J. Phys. Condens. Matter **7**, 8219 (1995)
40. J.R. Pinzón, A. Villalta-Cerdas, L. Echegoyen, Fullerenes, carbon nanotubes, and graphene for molecular electronics, in *Unimolecular and Supramolecular Electronics*, vol. 312 (Springer, Berlin/Heidelberg, 2012), pp. 127–74

41. O. Gunnarson, *Alkali-Doped Fullerides Narrow-Band Solids with Unusual Properties* (World Scientific, Singapore, 2004)
42. R. Verucchi, L. Aversa, M.V. Nardi, S. Taioli, S. a Beccara, D. Alfè, L. Nasi, F. Rossi, G. Salviati, S. Iannotta, Epitaxy of nanocrystalline silicon carbide on Si(111) at room temperature. J. Am. Chem. Soc. Commun. **134**, 17400–17403 (2012)
43. S. Taioli, G. Garberoglio, S. Simonucci, S. a Beccara, L. Aversa, M. Nardi, R. Verucchi, S. Iannotta, M. Dapor, D. Alfè, Non-adiabatic ab initio molecular dynamics of supersonic beam epitaxy of silicon carbide at room temperature. J. Chem. Phys. **138**, 044701 (2013)
44. L. Aversa, S. Taioli, M.V. Nardi, R. Tatti, R. Verucchi, S. Iannotta, The interaction of C_{60} on Si(111) 7×7 studied by supersonic molecular beams: interplay between precursor kinetic energy and substrate temperature in surface activated processes. Front. Mater. **2**, 46 (2015)
45. S. Taioli, M. Dapor, N.M. Pugno, New frontiers in multiscale modelling of advanced materials. Front. Mater. **2**, 71 (2015)
46. R. Tatti, L. Aversa, R. Verucchi, E. Cavaliere, G. Garberoglio, N.M. Pugno, G. Speranza, S. Taioli, Synthesis of single layer graphene on Cu(111) by C_{60} supersonic molecular beam epitaxy. RSC Adv. **6**, 37982–37993 (2016)
47. D. Haberer, D. Vyalikh, S. Taioli, B. Dora, M. Farjam, J. Fink, D. Marchenko, T. Pichler, K. Ziegler, S. Simonucci et al., Tunable band gap in hydrogenated quasi-free-standing graphene. Nano Lett **10**, 3360–3366 (2010)
48. D. Haberer, L. Petaccia, M. Farjam, S. Taioli, S. Jafari, A. Nefedov, W. Zhang, L. Calliari, G. Scarduelli, B. Dora et al., Direct observation of a dispersionless impurity band in hydrogenated graphene. Phys. Rev. B **83**, 165433 (2011)
49. S. Taioli, A. Paris, L. Calliari, Characterization of pristine and functionalized graphene on metal surfaces by electron spectroscopy, in *Graphene Science Handbook: Size-Dependent Properties*, vol. 5 (CRC Press/Taylor & Francis Group, Boca Raton, 2016), pp. 269–285
50. S. Taioli, Computational study of graphene growth on copper by first-principles and kinetic Monte Carlo calculations. J. Mol. Mod. **20**, 1–13 (2014)
51. G. Xu, X.-Q. Shi, R.Q. Zhang, W.W. Pai, H.T. Jeng, M.A. Van Hove, Detailed low-energy electron diffraction analysis of the (4×4) surface structure of C_{60} on Cu(111): seven-atom-vacancy reconstruction. Phys. Rev. B **86**, 075419 (2012)
52. G. Galli, F. Mauri, Large scale quantum simulations: C_{60} impacts on a semiconducting surface. Phys. Rev. Lett. **73**, 3471–3474 (1994)
53. X. Hu, K. Albe, R.J. Averback, Molecular-dynamics simulations of energetic C_{60} impacts on (2×1)–(100) silicon. Appl. Phys. **88**, 49–54 (2000)
54. A. Paris, S. Taioli, Multiscale investigation of oxygen vacancies in TiO_2 anatase and their role in memristor's behavior. J. Phys. Chem. C **120**, 22045–22053 (2016)
55. G. Kresse, J. Hafner, Ab initio molecular dynamics for liquid metals. Phys. Rev. B **47**, 558–561 (1993)
56. G. Kresse, J. Hafner, Ab initio molecular-dynamics simulation of the liquid-metal–amorphous-semiconductor transition in germanium. Phys. Rev. B **49**, 14251–14269 (1994)
57. A. Carpinteri, N.M. Pugno, One-, two- and three-dimensional universal laws for fragmentation due to impact and explosion. J. Appl. Mech. **69**, 854–856 (2002)
58. Z. Slanina, E. Osawa, Average bond-dissociation energies of fullerenes. Fullerene Sci. Technol. **5**, 167–175 (1997)
59. M.J. Allen, V.C. Tung, R.B. Kaner, Honeycomb carbon: a review of graphene. Chem. Rev. **110**, 132–145 (2010)
60. E.P. Randviir, D.A.C. Brownson, C.E. Banks, A decade of graphene research: production, applications and outlook. Mater. Today **17**, 426–432 (2014)
61. S. Signetti, S. Taioli, N.M. Pugno, 2D material armors showing superior impact strength of few layers. ACS Appl. Mater. Interfaces **9**, 40820–40830 (2017)
62. E. Lepore, F. Bosia, F. Bonaccorso, M. Bruna, S. Taioli, G. Garberoglio, A.C. Ferrari, N.M. Pugno, Spider silk reinforced by graphene or carbon nanotubes. 2D Mater. **4**, 031013 (2017)
63. A. Pedrielli, S. Taioli, G. Garberoglio, N.M. Pugno, Mechanical and thermal properties of graphene random nanofoams via molecular dynamics simulations. Carbon **132**, 766–775 (2018)

64. M. Azzolini, T. Morresi, K. Abrams, R. Masters, N. Stehling, C. Rodenburg, N.M. Pugno, S. Taioli, M. Dapor, Anisotropic approach for simulating electron transport in layered materials: computational and experimental study of highly oriented pyrolitic graphite. J. Phys. Chem. C **122**, 10159–10166 (2018)
65. A. Pedrielli, S. Taioli, G. Garberoglio, N.M. Pugno, Designing graphene based nanofoams with nonlinear auxetic and anisotropic mechanical properties under tension or compression. Carbon **111**, 796–806 (2017)
66. L.D. Landau, E.M. Lifshitz, *Statistical Physics* (Pergamon, Oxford, 1980)
67. R.E. Peierls, Bemerkungen über Umwandlungstemperaturen. Helv. Phys. Acta **7**, 81–83 (1934)
68. K.S. Novoselov, A.K. Geim, S.V. Morozov, S.V. Dubonos, Y. Zhang, D. Jiang, Room-temperature electric field effect and carrier-type inversion in graphene films. arXiv:cond-mat/0410631 (2004)
69. C. Tan, H. Zhang, Two-dimensional transition metal dichalcogenide nanosheet-based composites. Chem. Soc. Rev. **44**, 2713–2731 (2015)
70. P. Vogt, P. De Padova, C. Quaresima, J. Avila, E. Frantzeskakis, M.C. Asensio, A. Resta, B. Ealet, G. Le Lay, Silicene: compelling experimental evidence for graphenelike two-dimensional silicon. Phys. Rev. Lett. **108**, 155501 (2012)
71. X. Chen, Q. Yang, R. Meng, J. Jiang, Q. Liang, C. Tan, X. Sun, The electronic and optical properties of novel germanene and antimonene heterostructures. J. Mater. Chem. C **4**, 5434–5441 (2016)
72. L. Matthes, O. Pulci, F. Bechstedt, Massive Dirac quasiparticles in the optical absorbance of graphene, silicene, germanene, and tinene. J. Phys. Condens. Matter. **25**, 395305 (2013)
73. H. Aoki, M. Dresselhaus (eds.), *Physics of Graphene* (Springer, Berlin, 2014)
74. T. Morresi, A. Pedrielli, R. Gabbrielli, N.M. Pugno, S. Taioli, Structural, electronic and mechanical properties of all-sp^2 graphene allotropes: the specific strength of tilene parent is higher than that of graphene and flakene has the minimal density. arXiv:1811.01112 [cond-mat.mtrl-sci] (2018)
75. W. Fischer, E. Koch., Homogeneous sphere packings with triclinic symmetry. Acta Crystallogr. Sect. A **58**, 509–513 (2002)
76. H. Sun, S. Mukherjee, M. Daly, A. Krishnan, New insights into the structure-nonlinear mechanical property relations for graphene allotropes. Carbon **110**, 443–457 (2016)
77. S. Zhang, J. Zhou, Q. Wang, X. Chen, Y. Kawazoe, P. Jena, Penta-graphene: a new carbon allotrope. PNAS **112**, 2372–2377 (2015)
78. Y.J. Dappe, R. Oszwaldowski, P. Pou, J. Ortega, R. Pérez, F. Flores, Local-orbital occupancy formulation of density functional theory: application to Si, C, and graphene. Phys. Rev. B **73**, 235124 (2006)
79. I.A. Pasti, A. Jovanović, A.S. Dobrota, S.V. Mentus, Atomic adsorption on pristine graphene along the periodic table of elements – from PBE to non-local functionals. Appl. Surf. Sci. **436**, 433–440 (2018)
80. X.L. Sheng, H.-J. Cui, F. Ye, Q.-B. Yan, Q.-R. Zheng, G. Su, Octagraphene as a versatile carbon atomic sheet for novel nanotubes, unconventional fullerenes, and hydrogen storage. J. Appl. Phys. **112**, 074315 (2012)
81. F. Thorpe, I. Jasiuk, Proc. Math. Phys. Sci. **438**, 531–544 (1992)
82. S. Taioli, R. Gabbrielli, S. Simonucci, N.M. Pugno, A. Iorio, Lobachevsky crystallography made real through carbon pseudospheres. J. Phys. Condens. Matter. **28**, 13LT01 (2016)
83. A. Iorio, G. Lambiase, The Hawking-Unruh phenomenon on graphene. Phys. Lett. B **716**, 334–337 (2012)
84. M.M. Riegera, L. Steinbeck, I.D. White, H.N. Rojas, R.W. Godby, The GW space-time method for the self-energy of large systems. Comput. Phys. Commun. **177**, 211–228 (1999)
85. P. Umari, G. Stenuit, S. Baroni, Optimal representation of the polarization propagator for large-scale GW calculations. Phys. Rev. B **79**, 201104(R) (2009)
86. P. Umari, G. Stenuit, S. Baroni, GW quasiparticle spectra from occupied states only. Phys. Rev. B **81**, 115104 (2010)

87. M.S. Hybertsen, S.G. Louie, Electron correlation in semiconductors and insulators: band gaps and quasiparticle energies. Phys. Rev. B **34**, 5390–5413 (1986)
88. C. Friedrich, M.C. Müller, S. Blügel, Band convergence and linearization error correction of all-electron *GW* calculations: the extreme case of zinc oxide. Phys. Rev. B **83**, 081101R (2011)
89. J.P. Perdew, A. Zunger, Self-interaction correction to density-functional approximations for many-electron systems. Phys. Rev. B **23**, 5048–5079 (1981)
90. E.B. Barros, A. Jorio, G.G. Samsonidzef, R.B. Capazc, A.G. Souza Filhoa, J.M. Filhoa, G. Dresselhaus, M.S. Dresselhaus, Review on the symmetry-related properties of carbon nanotubes. Phys. Rep. **431**, 261–302 (2006)
91. H. Lin, J. Lagoute, V. Repain, C. Chacon, Y. Girard, J.-S. Lauret, F. Ducastelle, A. Loiseau, S. Rousset, Many-body effects in electronic bandgaps of carbon nanotubes measured by scanning tunnelling spectroscopy. Nat. Mat. **9**, 235–238 (2010)
92. R.B. Weisman, S.M. Bachilo, Dependence of optical transition energies on structure for single-walled carbon nanotubes in aqueous suspension: an empirical kataura plot. Nano Lett. **3**, 1235–1238 (2003)
93. G. Dukovic, F. Wang, D. Song, M.Y. Sfeir, T.F. Heinz, L.E. Brus, Structural dependence of excitonic optical transitions and band-gap energies in carbon nanotubes. Nano Lett. **5**, 2314–2318 (2005)
94. R. Saito, G. Dresselhaus, M.S. Dresselhaus, *Physical Properties of Carbon Nanotubes* (Imperial College Press, London, 1998)
95. J. Deslippe, M. Dipoppa, D. Predergast, M.V.O. Moutinho, R.B. Capaz, S.G. Louie, Electron-hole interaction in carbon nanotubes: novel screening and exciton excitation spectra. Nano Lett. **9**, 1330–1334 (2009)
96. M. Rohlfing, S.G. Louie, Electron-hole excitations and optical spectra from first principles. Phys. Rev. B. **62**, 4927–4944 (2000)
97. W. Kang, M.S. Hybertsen, Enhanced static approximation to the electron self-energy operator for efficient calculation of quasiparticle energies. Phys. Rev. B **82**, 195108 (2010)
98. T. Miyake, S. Saito, Quasiparticle band structure of carbon nanotubes. Phys. Rev. B **68**, 155423 (2003)
99. P. Avouris, Z. Chen, V. Perebeinos, Carbon-based electronics. Nat. Nano. **2**, 605–615 (2007)
100. M. Dapor, Mermin differential inverse inelastic mean free path of electrons in polymethylmethacrylate. Front. Mater. **2**, 27 (2015)
101. S. Taioli, S. Simonucci, L. Calliari, M. Dapor, Electron spectroscopies and inelastic processes in nanoclusters and solids: theory and experiment. Phys. Rep. **493**, 237–319 (2010)
102. S. Taioli, S. Simonucci, A computational perspective on multichannel scattering theory with applications to physical and nuclear chemistry. Annu. Rep. Comput. Chem. **11**, 191–310 (2015)
103. Y. Li, A. Chernikov, X. Zhang, A. Rigosi, H.M. Hill, A.M. van der Zande, D.A. Chenet, E.-M. Shih, J. Hone, T.F. Heinz, Measurement of the optical dielectric function of monolayer transition-metal dichalcogenides: MoS_2, $MoSe_2$, WS_2, and WSe_2. Phys. Rev. B **90**, 205422 (2014)
104. J. Daniels, C.V. Festenberg, H. Raether, K. Zeppenfeld, *Optical Constants of Solids by Electron Spectroscopy*. Springer Tracts in Modern Physics, vol. 54 (Springer, Berlin, 1970), pp. 77–135
105. H. Raether, Excitation of plasmons and interband transitions by electrons, vol. 88 (Springer, Berlin, 1980)
106. S. Baroni, R. Resta, Ab initio calculation of the macroscopic dielectric constant in silicon. Phys. Rev. B **33**, 7017–7021 (1986)
107. M. Dapor, G. Garberoglio, L. Calliari, Energy loss of electrons impinging upon glassy carbon, amorphous carbon, and diamond: comparison between two different dispersion laws. Nucl. Instrum. Methods Phys. Res. B **352**, 181–185 (2015)
108. M. Dapor, L. Calliari, M. Filippi, Computational and experimental study of π and $\pi + \sigma$ plasmon loss spectra for low energy ($<1000\,\mathrm{eV}$) electrons impinging on highly oriented pyrolitic graphite (HOPG). Nucl. Instrum. Methods Phys. Res. B **255**, 276–280 (2007)

109. R. Garcia-Molina, I. Abril, I. Kyriakou, D. Emfietzoglou, Inelastic scattering and energy loss of swift electron beams in biologically relevant materials. Surf. Interface Anal. **49**, 11–17 (2017)
110. E. Runge, E.K.U. Gross, Density-functional theory for time-dependent systems. Phys. Rev. Lett. **52**, 997–1000 (1984)
111. C.A. Ullrich, *Time-Dependent Density Functional Theory: Concepts and Applications*. Oxford Graduate Texts (Oxford University Press, Oxford, 2012)
112. G. Onida, L. Reining, A. Rubio, Electronic excitations: density-functional versus many-body Green's-function approaches. Rev. Mod. Phys. **74**, 601–659 (2002)
113. L. Hedin, New method for calculating the one-particle green's function with application to the electron-gas problem. Phys. Rev. **139**, A796–A823 (1965)
114. S.L. Adler, Quantum theory of the dielectric constant in real solids. Phys. Rev. **126**, 413–420 (1962)
115. N. Wiser, Dielectric constant with local field effects included. Phys. Rev. **129**, 62–69 (1963)
116. R.H. Ritchie, Plasma losses by fast electrons in thin films. Phys. Rev. **106**, 874–881 (1957)
117. M. Dapor, *Electron–Beam Interactions with Solids* (Springer, Berlin, 2003)
118. H. Nikjoo, S. Uehara, D. Emfietzoglou, *Interaction of Radiation with Matter* (CRC Press/Taylor & Francis Group, Boca Raton, 2012)
119. H. Nikjoo, D. Emfietzoglou, T. Liamsuwan, R. Taleei, D. Liljequist, S. Uehara, Radiation track, DNA damage and response–a review. Rep. Prog. Phys. **79**, 116601 (2016)
120. M. Dapor, Energy loss of fast electrons impinging upon polymethylmethacrylate. Nucl. Instrum. Methods Phys. Res. B **352**, 190–194 (2015)
121. F. Yubero, S. Tougaard, Model for quantitative analysis of reflection-electron-energy-loss spectra. Phys. Rev. B **46**, 2486–2497 (1992)
122. E. Shiles, T. Sasaki, M. Inokuti, D.Y. Smith, Self-consistency and sum-rule tests in the Kramers-Kronig analysis of optical data: applications to aluminum. Phys. Rev. B **22**,1612–1628 (1980)
123. R. Garcia-Molina, I. Abril, C.D. Denton, S. Heredia-Avalos, Allotropic effects on the energy loss of swift H^+ and He^+ ion beams through thin foils. Nucl. Instrum. Methods Phys. Res. B **249**, 6–12 (2006)
124. S. Tanuma, C.J. Powell, D.R. Penn, Calculations of electron inelastic mean free paths. IX. Data for 41 elemental solids over the 50 eV to 30 keV range. Surf. Interface Anal. **43**, 689–713 (2011)
125. S. Sharma, J. Dewhurst, A. Sanna, E.K.U. Gross, Bootstrap approximation for the exchange-correlation kernel of time-dependent density-functional theory. Phys. Rev. Lett. **107**, 186401 (2011)
126. S. Waidmann, M. Knupfer, B. Arnold, J. Fink, A. Fleszar, W. Hanke, Phys. Rev. B **61**, 10149–10153 (2000)
127. J. Harl, The linear response function in density functional theory: optical spectra and improved description of the electron correlation. Ph.D. thesis, Universitat Wien (2008)
128. A.B. Bortz, M.H. Kalos, J.L. Lebowitz, A new algorithm for Monte Carlo simulation of Ising spin systems. J. Comput. Phys. **17**, 10–18 (1975)
129. M. Dapor, *Transport of Energetic Electrons in Solids*, 2nd edn. (Springer, Berlin, 2017)
130. M. Dapor, Role of the tail of high-energy secondary electrons in the Monte Carlo evaluation of the fraction of electrons backscattered from polymethylmethacrylate. Appl. Surf. Sci. **391**, 3–11 (2017)
131. S. Taioli, S. Simonucci, M. Dapor, Surprises: when ab initio meets statistics in extended systems. Comput. Sci. Discov. **2**, 015002 (2009)
132. S. Taioli, S. Simonucci, L. Calliari, M. Filippi, M. Dapor, Mixed ab initio quantum mechanical and MonteCarlo calculations of secondary emission from SiO_2 nanoclusters. Phys. Rev. B **79**, 085432 (2009)
133. S. Taioli, A bird's eye view on the concept of multichannel scattering with applications to materials science, condensed matter, and nuclear astrophysics. Front. Mater. **2**, 71 (2015)

134. M.S. Green, Markoff random processes and the statistical mechanics of time-dependent phenomena. II. Irreversible processes in fluids. J. Chem. Phys. **22**, 398–413 (1954)
135. R. Kubo, Statistical-mechanical theory of irreversible processes. I. General theory and simple applications to magnetic and conduction problems. J. Phys. Soc. Jpn. **12**, 570–586 (1957)
136. A. Pedrielli, S. Taioli, G. Garberoglio, N.M. Pugno, Gas adsorption and dynamics in pillared graphene frameworks. Microporous Mesoporous Mater. **257**, 222–231 (2018)
137. G. Garberoglio, N.M. Pugno, S. Taioli, Gas adsorption and separation in realistic and idealized frameworks of organic pillared graphene: a comparative study. J. Phys. Chem. C **119**, 1980–1987 (2014)
138. A. Battisti, S. Taioli, G. Garberoglio, Zeolitic imidazolate frameworks for separation of binary mixtures of CO_2, CH_4, N_2 and H_2: a computer simulation investigation. Microporous Mesoporous Mater. **143**, 46–53 (2011)
139. G. Garberoglio, S. Taioli, Modelling flexibility in metal–organic frameworks: comparison between density-functional tight-binding and universal force field approaches for bonded interactions. Microporous Mesoporous Mater **163**, 215–220 (2012)
140. L. Lu, P.S.E. Yeo, C.W. Gan, P. Wu, K.P. Loh, Transforming C_{60} molecules into graphene quantum dots. Nat. Nanotechnol. **6**, 247–252 (2011)
141. N. Swami, H. He, B.E. Koel, Polymerization and decomposition of C_{60} on Pt(111) surfaces. Phys. Rev. B **59**, 8283–8291 (1999)
142. E.P. Randviir, D.A.C. Brownson, C.E. Banks, A decade of graphene research: production, applications and outlook. Mater. Today **17**, 426–432 (2014)